Dissertation
submitted to the
Combined Faculties of Natural Sciences and for Mathematics
of the Ruperto-Carola University of Heidelberg, Germany
for the degree of
Doctor of Natural Sciences

presented by Master-diploma Physicist Mikhail Rashev
born in Vyborg, Russia
Oral examination: 16.02.2005

A new Time-of-flight Spectrometer for Impact Generated Ions

Referees	Prof. Dr. Eberhard Grün
	Prof. Dr. Karlheinz Meier

Abstract

This thesis deals with the development of a time-of-flight mass spectrometer (Large Area Dust Mass Analyzer). This next generation instrument will have a large sensitive area($0.1m^2$) in order to achieve a higher number of dust impacts and a mass resolution $\frac{m}{\Delta m} \geq 100$ which allows the identification of the most abundant elements in a dust particle.

In order to study the hypervelocity impact process as well as to apply new components for mass analyzer the laboratory set-up was built. It has a reflectron in order to compensate initial ion energies and a microchanel plate detector as an ion detector.

The Large Area Mass Analyzer has been simulated. The sensitive area of the instrument is about $0.1m^2$. The mass resolution varies in the range 150-200. The design improvements allow us to incorporate the trajectory sensor in order to determine the velocity and mass of the dust particles. A simulating software as well as analytical calculations were applied in order to obtain the geometrical configuration. Both a microchannel plate detector and an ion-to-electron converter were designed for the ion detector.

Zusammenfassung

Die vorliegende Arbeit behandelt die Entwicklung eines Flugzeitmassenspektrometers (*Large Area Mass Analyzer, LAMA*) zur chemischen Analyse von Staubteilchen im Weltraum. Dieses Instrument der nächsten Generation wird eine große Detektorfläche($0.1m^2$) haben, um möglichst viele Staubteilcheneinschläge zu erhalten. Die Massenauflösung von $\frac{m}{\Delta m} \geq 100$ erlaubt es, die häufigsten in einem Staubteilchen enthaltenen Elemente zu identifizieren.

Um den Einschlagsvorgang eines Hochgeschwindigkeitsteilchens zu untersuchen und um neu entwickelte Komponenten des Massenanalysators zu testen, wurde ein Labormodell entwickelt. Es verfügt über ein Reflektron zur Kompensation der Anfangsenergie der Ionen. Eine Mikrokanalplatte dient als Ionendetektor.

Der *Large Area Mass Analyzer* wurde simuliert. Die empfindliche Fläche des Instruments beträgt ca. $0.1m^2$. Die Massenauflösung liegt im Bereich von 150 - 200. Verbesserungen in der Konstruktion ermöglichen den Einbau eines Trajektoriensensors zur Bestimmung von Geschwindigkeit und Masse der Teilchen. Zur geometrischen Konfiguration des Instruments wurden sowohl numerische Simulationen als auch analytische Berechnungen durchgeführt. Die Mikrokanalplatte und der neu entwickelte Ion-Elektron-Konverter bilden den Ionendetektor des LAMA.

Contents

Chapter 1

Introduction

1.1 Galactic Interstellar Dust

Interstellar dust became a topic of astrophysical research in the early 1930s when the extinction (absorption and scattering) of starlight in the interstellar medium (ISM) was recognized.

A weak polarization of starlight revealed that the dust grains embedded in the interstellar medium must be elongated and have a preferential orientation in space as well. Infrared absorption bands detected in the late 1960s allowed one of the first analysis of the composition of the grains. From optical observations, dust models were proposed based upon assumptions on the chemical composition,the shape and the size distributions of grains [1] [2], [3].

Most material contained in the Earth and the other planets today resided in galactic interstellar dust grains 5×10^9 years ago before it was altered during the process of planetary formation. Interstellar dust is believed to originate from the extended atmospheres of evolved stars (e.g. carbon-rich stars, red giant stars) or supernovae. These sources eject dust with characteristic individual chemical and isotopic signatures into the interstellar medium which is modified during the grains' evolution in interstellar space. Presolar grains have been identified in primitive meteorites: e.g. diamonds, graphite, silicon carbide or corundum grains. The identified grains, however, represent only a very small fraction of the total material that went into the protoplanetary disk. The composition of the grains is largely unknown. Their analysis of interstellar dust grains can give important insights into the formation process of our planetary system[4], [5],[6] .

Interstellar dust grains are closely connected to the chemical evolution of the Galaxy and the Universe. The dust mass in the Galaxy is grossly proportional to the total amount of heavy elements and interstellar grains carry most of the mass of heavy elements in the interstellar medium. Dust contains about 40% of the mass of heavy elements in our Galaxy[7], [8], [9].

Our planetary system is not isolated in space therefore one expects penetration of interstellar dust.

1.2 Dust in the Solar System

Interstellar dust in the planetary system was identified with the Ulysses spacecraft about 10 years ago [10, 11]. Ulysses orbits the Sun in an orbit nearly perpendicular to the ecliptic plane and carries a highly sensitive dust detector on board which measures micrometer and submicrometer dust particles [12]. A nearly constant flux of interstellar grains has been observed at all ecliptic latitudes while the flux of interplanetary grains varies strongly with latitude. Within the measurement accuracy the flow direction of interstellar dust coincided with that of the interstellar helium gas also measured with Ulysses [13] and the particle speed exceeded the local escape speed from the solar system. The Ulysses measurements of interstellar dust were later confirmed by the twin of the Ulysses dust detector on board the Galileo spacecraft [14].

In addition to galactic interstellar dust the Ulysses and Galileo dust experiments allowed to study the interplanetary dust complex [15] which could only be studied with astronomical observation techniques before. This lead to the identification of various dust populations [16, 17, 18]. Streams of tiny of electromagnetically interacting dust grains with sizes of about 10 nanometers were discovered by Ulysses [10] and later confirmed by Galileo [19]. The Galileo measurements showed that the streams originate from Jupiter's volcanically active moon Io and allowed to study various dust phenomena in the Jovian system like, most notably, dust clouds surrounding the Galilean satellites [20] and Jupiter's dusty rings including Jupiter's gossamer ring.

The Cassini spacecraft which is presently on its way to Saturn carries an upgrade of the Galileo and Ulysses dust detectors. In addition to particle speeds and masses it also measures the charges carried by the particles and the coarse chemical composition [21].

The cometary missions Giotto, VeGa 1 and 2 studied Halley's comet in the 1980s. They were equipped with time-of-flight mass spectrometers for the chemical analysis of Halley's dust. These measurements showed that the abundances of heavy elements in Halley's dust very closely resemble that of the solar photosphere. In addition, the Hally measurements allowed studies of outflow mechanisms and the thermophysical properties of dust and gas in the cometary coma. Space missions to other comets (Stardust and Rosetta) will provide new insights into the properties and evolution of cometary dust in the future.

Analizing physical and chemical proporties of interstellar dust one can deduce evolution of our Galaxy and the Universe. Our group develop dust sensors. New one consists of two parts. Trajectory sensor determines a dust partricle trajectory, mass and velocity. The second part, the mass analyzer defines composition of a dust particle.

1.3 Scope of this Thesis

The task of this thesis is to develop the chemical mass analyzer of dust particles. In this work I discuss the time-of-flight spectrometer for chemical analysis of cosmic dust particles in space.

The measurement technique is based on the impact-ionization process: dust particles hitting a metal target with very high speed evaporate and the resulting plasma cloud is measured. Typical impact speeds accessible in the laboratory range from a few kilometers per second to 50 km s.

Particles in space can be faster. The impact plasma is separated by an electric field and the electrons and ions are registered at the target and at an ion collector, respectively. Three instruments of this type are presently being operated on the Cassini, Galileo and Ulysses spacecraft by the Heidelberg dust research group.

The facilities for dust research available at the Max-Planck-Institut for Nuclear Physics in Heidelberg as well as former instruments and impact ionization method will be described in Chapter 2. A high-resolution mass analyzer was developed in order to study the initial conditions of the ions. This is described in Chapter 3. A new reflectron-type configuration was developed for the next generation of dust instruments to be flown on the Dune mission. The main goal of Dune will be the analysis of galactic interstellar dust. An advantage of the reflectron is that the different initial conditions of the ions after the particle impact onto the target can be compensated. This is described in Chapter 4. Some improvements that were done to the Large Area Mass Analyzer and the steps necessary to build such an instrument are discussed in Chapter 5. Chapter 6 is a conclusion to all this work. Several instrument configurations were tested to optimize mass resolution and spatial focusing. Pictures of the optimized High Resolution Mass Analyzer are shown in Appendix A. The Dust Analyzers were simulated with the SIMION 7.0 software. The geometry configurations are defined in text files which served as input for SIMION. These files which describe the geometry are given in Appendices B and C. The files which optimize the electrode voltages are also shown in Appendix C.

Chapter 2

Experimental methods for dust research

The world is full of dust. We see it every day around us. Even when looking at the sky we cannot avoid it as well. From time to time dust particles enter the Earth's atmosphere. Then they are altered or even destroyed when entering.

It is possible to analyze the dust particles either on Earth or in cosmic space. Heidelberg dust research group investigates the cosmic dust in space. If dust particle is analyzed in space it is possible to determine the particle trajectory and the particle composition. If it is measured on the Earth the result will be different.

By the term "dust" we mean tiny solid particulates with sizes in the range of about 0.1 to 10 μm. These dust particles are characterized by their properties such as mass, composition, and velocity which can reach hundreds of km/s. As the particle is charged the mass and velocity of a particle can be measured when the particle passes a system of wires. The composition can be measured through particle destruction. When a hypervelocity dust particle encounters a target it splits into fragments creating ions and molecules. This method is called impact ionization[22]. The resulting ions are accelerated and can be detected. Via known time-of-flight the masses of the ion species can be determined. This kind of dust sensors flew on board Helios [23] and are still in operation on board the Galileo[24], Ulysses[25] and Cassini-Huygens[26] missions.

The Heidelberg dust research group operates in-situ instruments for hyper-velocity impact detection. Several instruments for dust investigations were built and are operating now in Heidelberg. It gives unique possibility to watch for dust in 'on-line' regime. In the laboratory dust-like particles or laser shot can be used for instrument calibration or to investigate the hypervelocity impact. The laboratory set-up was also used to test mass analyzer described in chapter 3.

2.1 Impact ionization method

A general theory describing the hypervelocity impact process is not developed yet. Therefore one can describe the process generally and then introduce a theoretical approach.

All dust sensors developed in our group are based on the hyper-velocity impact of a dust particle upon a solid target of dust sensor. The dust particle hits the the analyzer target and is fragmentated. The shock wave produced by the impact creates positive ions and free electrons,

in a dense expanding plasma cloud. The remaining atomic and molecular ions, expanding behind the electrons, emerge from a highly positively charged region. As long as a dense plasma cloud exists the ions inside the plasma are isolated from the influence of the electric field. Afterwards the plasma cloud expands and the particles inside perform mutual collisions. The interaction of the electric field with individual ions becomes a dominant process, and the ions are accelerated by the electric field and are focused onto the ion detector. The electrons give a so-called 'start' signal and the ions give 'stop' signal. The mass of the ions is defined via a flight time from the target to the ion detector. Figure 2.1 shows a case when the particle velocity $v > 50$km/s and the particle is completely vaporized [27]. At the top is the part of the mass analyzer including a target and an acceleration grid. The dust particle is completely separated into single ions. The

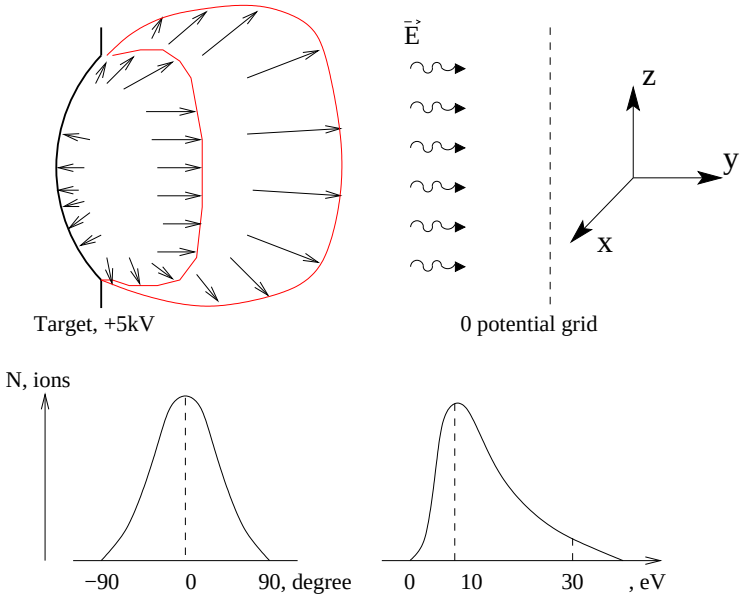

Figure 2.1: A tiny dust grain hits the target. The grain vaporizes and ionizes a small volume of the target. The expanding plasma cloud is shown. The bottom shows a possible energy and angular distribution of the ions.

arrows show ion velocities when the ion cloud expands. On the bottom a possible ion energy and angle distributions are shown.

The impact of the dust particle upon the solid target can be described using a hydrodynamical approach. The particle and the target are assumed to be a fluid with assigned velocities u_i to each fluid particle. At this point one can introduce density ρ, pressure p, specific energy e and temperature T using an assumption about dust particle velocity and mass as well as a transfer of kinetic energy to internal energy of particle-target material. Then an evolution of these values obeys these laws

$$\frac{\partial \rho}{\partial t} + \nabla \cdot \rho u = 0 \tag{2.1}$$

$$\frac{\partial u}{\partial t} \cdot \nabla u = -\frac{1}{\rho} \nabla p \tag{2.2}$$

$$\frac{de}{dt} + p\frac{dV}{dt} = Q \tag{2.3}$$

Where $V = 1/\rho$ is the specific volume and Q is the energy generated by the external sources per unit mass of the material and per unit time. It is assumed that Q is known. The internal energy e can be expressed in terms of density and pressure $e = f(\rho, p)$. So there are five unknowns(ρ, v_x, v_y, v_z, p) and five equations. Usually the energy is expressed via T and the task is to find the so-called equation of state $p = f(T, \rho)$ that can be found experimentally. Some of the existing models use the Thomas-Fermi equation [28] in order to describe an equation of state. Then the above equation should be carefully solved (numerically) as even for small changes in time and spatial steps the gradient can take on high values. Because of this, the calculations are extremely difficult and they are highly dependent on material structure(both dust particle and target).

In fact the most interesting points here are ion energy and angle distributions since the dust analyzers are strongly dependent on it. Those ranges can also be found experimentally using time-of-flight method and retarding fields [29]. For a wide range of dust particle velocity the initial ion energy distribution is between 0 and 50eV and the angle distribution is of $cos\alpha$ law due to the normal vector of the target. Such assumptions to the ions were made to design new analyzers: laboratory model and Large Area Mass Analyzers.

The impact ionization method used for all dust sensors of our group. Some of those are described in following section.

2.2 Former dust instrumentation

The Heidelberg dust research group has a long tradition in building dust sensors that define charge, mass , velocities and chemical composition of dust particles. In this section three dust sensors are considered (DDS, CDA, new dust telescope). When viewing these sensors one can note some similar features. Each following sensor has similar features and improved characteristics.

The Galileo, Ulysses and Gorid [30] instruments are very similar instruments. Fig. 2.2 shows a schematic drawing of this instrument type. The instruments consist of a hemispherical target and three entrance grids. The entrance grids consist of two grounded and one measurement grid, and the target has a 0.1 mm thick gold coating. The ion grid and the ion detector(channeltron) are located in the center of the target. The particles enter the detectors through a variety of grids. Since dust particles in space carry an electrical charge (surface potential of a few volts) the grids in front of the detectors measure the induced charge of the particle. By this means the speed and charge of the particles can be determined. The maximum sensitive area (for particles moving parallel to the sensor axis) is 0.1 m^2. Upon impact the particle produces a plasma, whose charge carriers are separated by an electric field between the target and the ion collector. Negative charges (mainly electrons) are collected at the target, the positive charges are collected partly by the ion collector and partly by a channeltron. The DDS measures the mass, speed, flight direction and electric charge of individual particle. The objective of the Galileo dust experiment

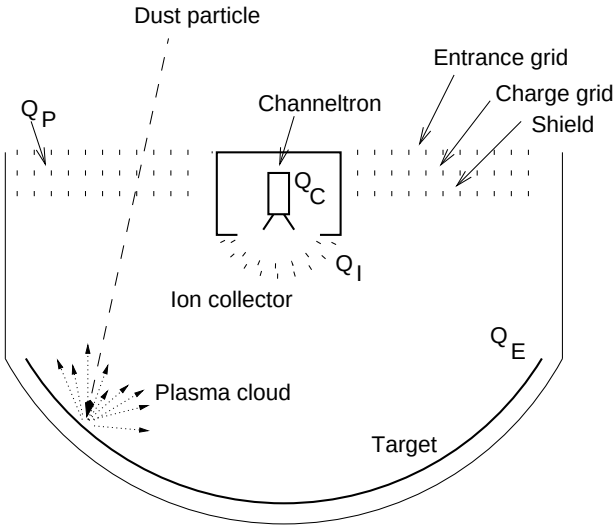

Figure 2.2: The Dust Detector System (DDS). There are three grids at the front end. A charged dust particle induces a charge on the "charge grid" while passing the grid segment. All particles are detected by a hemispherical impact target. During the impact process the particle is destroyed and an impact plasma and other fragments and neutral particles are generated. The ions and electrons are separated by an electric fi eld and are detected by charge sensitive amplifi ers attached to the target and to the ion grid. The pulse shape and amplitude determines the speed and mass of the impacting dust grain.*This type of instrument does not have a Chemical Analyzer providing a time-of-flight mass spectrum.*

is to investigate the physical and dynamical properties of small dust particles $10^{-16} - 10^{-6} g$ in the Jovian environment.

Next dust sensor Cassini has improved sensitivity and can determine a chemical composition of dust particles. Fig. 2.3 shows a sketch of the Cassini Cosmic-Dust-Analyzer (CDA). The Cosmic Dust Analyzer was developed for the investigations of dust in the vicinity of Saturn [21]. The Cosmic-Dust-Analyzer (CDA) is mounted on its perimeter. CDA consist of a large ($0.1\ m^2$) hemispherical impact ionization detector with a central ion collector and a Chemical Analyzer Target incorporated in the center of the big impact target. In contrast, DDS has only a trajectory sensor and no Chemical Analyzer. DDS can determine the trajectory, the charge of the particle and its velocity. CDA in addition has a Chemical Analyzer. It is situated in the center of the target. The sensitive area of the Chemical Analyzer is $100 cm^2$.

New dust telescope integrates a Trajectory Sensor and a Chemical Analyzer. The possible configuration of the new dust sensor is shown in Figure 2.4. The sensitive area of the Chemical Analyzer should be as high as $0.1 m^2$ instead of $0.01 m^2$ on CDA. An important improvement of this instrument is a reflectron implementation which compensates the difference of initial ion energies and hence it increases the mass resolution. As well as CDA it incorporates trajectory sensor and can define mass and velocity of dust particles.The trajectory sensor has a sensitivity 10 times bigger than for CDA. The detailed description of new Large Area Mass Analyzer (LAMA) will be done in chapters four and five.

When the dust sensor is designed and is manufactured the calibration has to be done in order

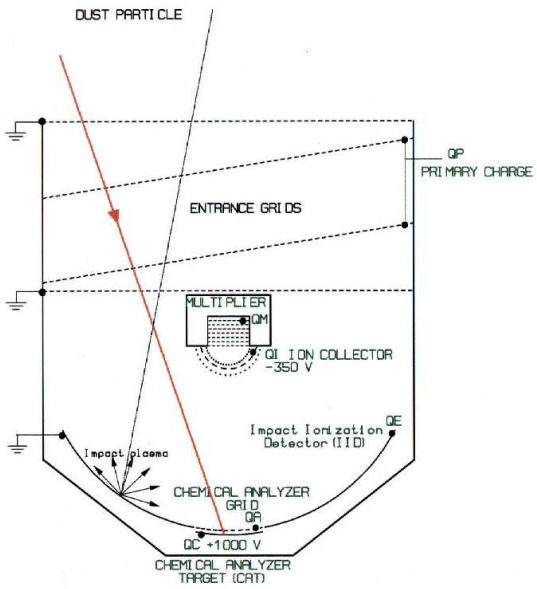

Figure 2.3: The Cosmic-Dust-Analyzer (CDA). The instrument consists of two components: the High-rate detection system (HRD) and the Dust Analyzer. The High rate detection system employs PVDF foils and determines the particle mass and the velocity. The Dust Analyzer determines the electrical charge, speed, mass and chemical composition of impacting particles. *There is a Chemical Analyzer with a target diameter of 16 cm.*

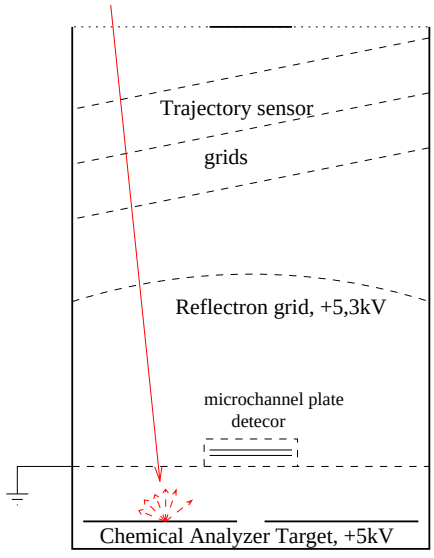

Figure 2.4: The DUNE design study. The sensitivity of the trajectory sensor will be increased by one order of magnitude comparing to CDA. *The entire area of the target works as a Chemical Analyzer. The mass resolution is higher than 100 and will allow to identify most of the elements occurring in space.*

to know how parameters of electrical signals correspond to the dust particle measured. The facility for sensors calibration are discussed in next section

2.3 Facility for instrument calibration

The dust research group at the Max-Planck-Institut for Nuclear Physics has a facility to simulate a hyper-velocity dust impact that allows investigation of the hypervelocity impact and calibrate dust sensors for in-situ analyses. The dust accelerator can accelerate the micrometer sized particles to speeds up to 50 km/s. A schematic drawing is shown in Figure 2.5. This technique is based on the acquisition of kinetic energy by a particle of mass m and positive charge q moving through a potential U, thus

$$\frac{mv^2}{2} = qU.$$

The accelerator uses a Van-de-Graaf high-voltage generator which produces an acceleration voltage of 2MV. The potential drops to ground via a cascade of equipotential rings. This scheme provides the electric field gradient along the accelerator beam line. The dust particles are charged in a dust source located in the generator terminal which is at the positive potential U of 2MV with respect to electrical ground. When particles are passing by the detectors 1 and 2 the charge q and velocity v are calculated. Thus the mass is defined using the relation $m = 2qU/v^2$. The high vacuum system provides a pressure of $10^4 - 10^7$ Pa inside the entire volume of the accelerator beam line.

The major part of the acceleration facility is the dust source providing dust-like particles of different materials. A new dust source [31] increases the material range. The Figure 2.6 shows the new dust source and principles of its working are shown below. Electrically conducting dust particles are contained in the reservoir of the dust source as a powder. In the reservoir center a 1 mm needle is located. The needle and the reservoir are in a potential of 15kV. The particles are blown up by pulses of the high voltage between the reservoir and the needle. Particles touching the needle are extracted from the reservoir in the direction of the electric field (along the beam line). The projectile materials cover a wide range of materials existing in space [32]. It is possible to accelerate Aluminum Al, Carbon C, Sodium Na, contaminated carbon $C-Na$, Iron Fe, Polyanlin coated polystyrene latex, $PANi-PS-Latex$, Polypyrrole coated polystyrene latex $PPY-PS-Latex$ and some other materials. The iron dust particles are shown in Figure 2.7 as an example.

Another possibility to simulate an impact of cosmic dust particle is by a laser shot [34]. Like a hypervelocity dust particle impact the focused laser spot creates a high density and high temperature state resulting in a vaporization and ionization of the surface region (Figure 2.8). The vapor consists of clusters, molecules, ions and electrons. The fragments leaving the impact region in different directions take away some energy. Eventual thermalization of the fragments occur via mutual collisions, typically within a distance of a few microns from the impact position [35].

In this case time-of-flight spectra will show features of the target material and contaminations. The laser has energy in a pulse of $3 \times 10^{-4} J$. Pulse duration up to 12ns is similar to the impact

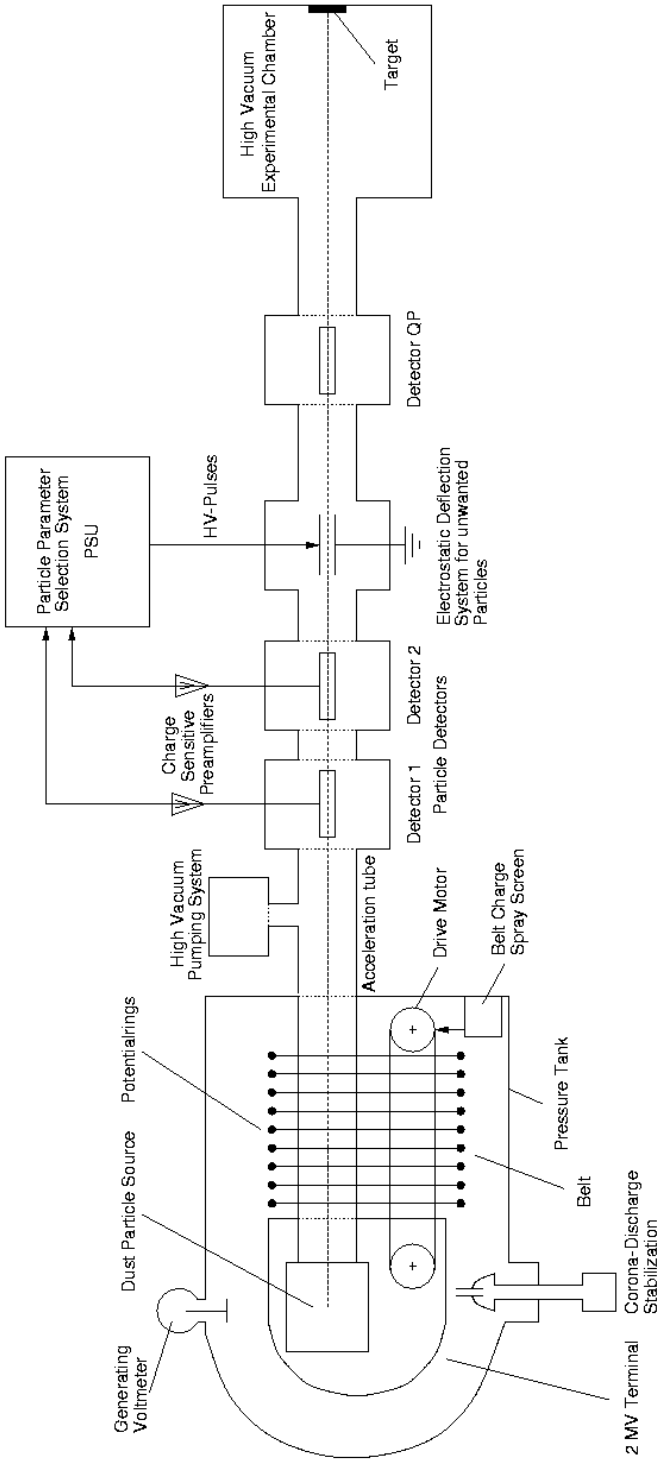

Figure 2.5: The Van-de-Graaf generator and the Heidelberg dust accelerator. The particle selection unit (PSU) and the experiment chamber are also shown.

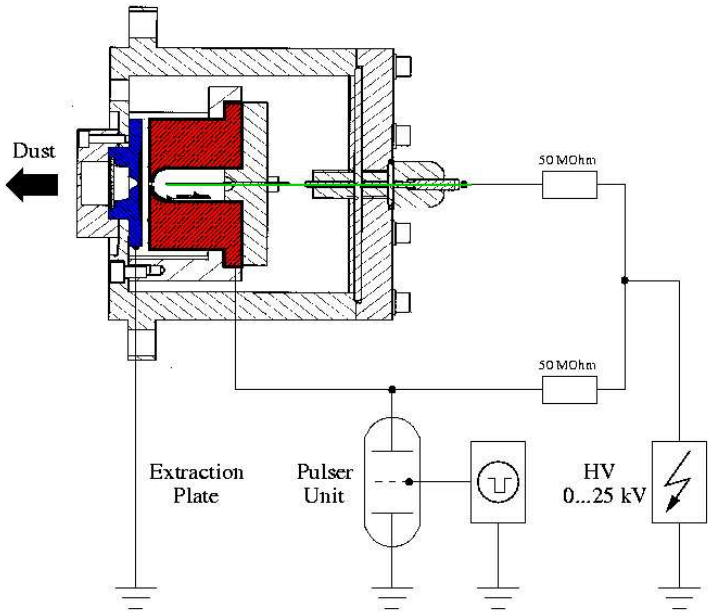

Figure 2.6: The new dust source with attached electronics. The dust in the reservoir is shown in black. The dust particles are finally charged by touching the needle and are extracted by the grounded extraction plate (the electrical ground is 2 MV high). The new dust source allows us to extract a variety of different dust materials.

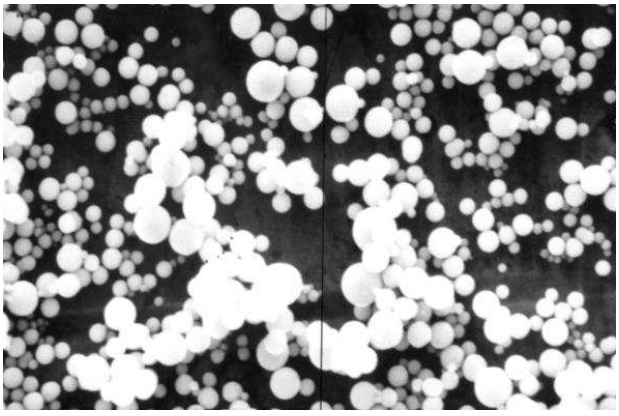

Figure 2.7: The iron dust particles used by the Heidelberg dust accelerator. The size of the dust particle varies from 0.1 to 3 μm. There is a similarity of this particles to iron-nickel meteorites [33].

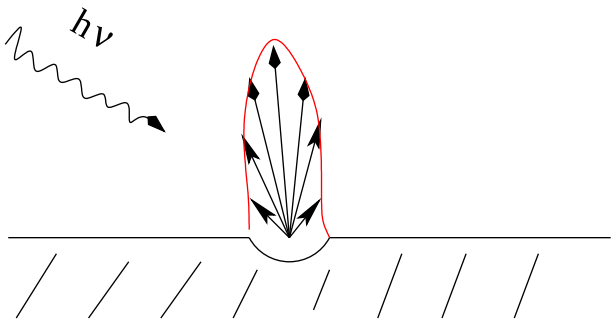

Figure 2.8: The dust particle impact process simulated by laser pulse. The incoming laser beam photons ionize and vaporize a region of the target surface material. The generated ion cloud is expanding. The arrows are ion velocities and the surrounding curve outlines a boundary of the ion cloud at a defined time.

time which is of a few ns. In fact it is much easier to handle the laser set-up. The energy of the laser can be adjusted in a wide range by changing the beam intensity. Considerably large number of events can be easily achieved.

Thus using the accelerator set-up and the laser set-up one can both calibrate the dust sensors and investigate the hypervelocity impact process

2.4 Conclusion

Heidelberg research group has a line of dust sensors for dust particles identification. Each new sensor improve characteristics of previous one. Last instruments have a mass analyzer in order to get chemical analyses of dust particles.

In order to build the chemical mass analyzer with high mass resolution the initial ion conditions formed during the impact have to be determined. Those values could be found either theoretically or using experimental methods.

For the calibration of dust sensors and investigation of the hypervelocity impacts the dust laboratory has the accelerator accelerating a wide range of different materials. Using the laser set-up one can depose the energy to the target which far beyond that reached by the accelerator. This equipment was also used to test simulated high resolution mass analyzer described in the proceeding chapter.

Chapter 3

High resolution chemical dust analyzers

In this chapter the mass analyzers with reflectron will be considered. In order to design mass analyzer of large area and high mass resolution several configurations were were built and simulated (PIA.PUMA, Dustbuster, Swedish configuration, Strong mirror configuration). The computer based models were built in order to find the mass resolution and the ion transmission. The goal of this simulation was to gain knowledge about critical elements of geometry configuration for large area mass analyzer. When considering PIA/PUMA mass analyzer I will discuss some crucial elements such as a modeling method, an ion detector and geometric configuration. Then the simulated data are compared to experimental data.

In different research groups a trend to employ a reflectron to the mass analyzers can be drawn. This implementation can significantly improve a mass resolution. Several dust mass spectrometers have been flown in space missions. The Helios [36] and Cassini [21] mass spectrometers were of a simple linear drift tube type and had low to medium mass resolutions ($\frac{M}{\Delta M} \leq 50$). The dust mass spectrometers PIA and PUMA [27] flown to comet Halley by the Giotto and VeGa missions were of the reflectron type [37] which provided high resolution mass spectra ($\frac{M}{\Delta M} \geq 100$). The Stardust CIDA instrument [38] is of the same type. Table 3.1 shows implementations of time-of-flight mass spectrometers in space. In last years several design studies of

Mission	launch date	Sensitive area	Mass resolution	Type
		(cm^2)	$\frac{M}{\Delta M}$	
Helios	1974	2×100	5-20	1 m linear drift tube
Cassini	1997	200	20-50	0.2 m linear drift tube
Giotto, VeGa	1985	5	100	1 m reflectron
Stardust	1999	90	100	1 m reflectron

Table 3.1: Implementations of Time-of-flight Mass Spectrometers in space.

new dust analyzers were done in various dust research groups. All of them employ the reflectron configuration. Svedhem and Oren [39] employ a two stage reflectron design with about 200 cm^2 target area, while Austin et al. [40] study a grid-less reflectron design of $65cm^2$ impact area. Both concepts will be discussed below.

3.1 Earlier geometric configurations

The last designs of dust analyzers have a reflectron which significantly increases the mass resolution. In this section mass analyzers with a reflectron are discussed. This was my first task to compare existing geometries and to improve them. In order to satisfy requirements for large area mass analyzer I increased area of impact target of these geometries(except PIA/PUMA). The first dust analyzer that has a reflectron was a PIA/PUMA . This instrument has a small sensitive area and devoted to measure dust particles near their source(comets). Far from the dust sources the dust flux is low. In order to get significant number of the particles the sensitive area should be increased. Three such designs with increased sensitive area are briefly discussed below. Another mass analyzer is discussed in details. This PIA/PUMA prototype has new design and is used for laboratory investigations. At the end of this chapter the simulated spectra are compared with measured ones.

3.1.1 PIA/PUMA

The advantage of PIA/PUMA is a high mass resolution and that the regions of the PIA/PUMA are well distinguished. The fig. 3.1 shows simulated PIA.PUMA prototype which is different of original design. One can clearly see the target region, the two field free regions, the reflectron and the detector volume. The disadvantage is the small sensitive area. However the analyzer has high mass resolution and can be used for investigations of the impact process, reflectron and ion detector. The laboratory had a vessel of the PIA/PUMA shape with the reflectron inside. Using such volume restrictions and positions of auxiliary flanges the analyzer was simulated and then was built. The objectives of the laboratory model are:

- the investigation of the initial impact conditions of the impact plasma such as the ion energy distribution and the ion angular distribution.

- the study of the correlation of SIMION simulations and measured data.

The mechanical design is a heritage of the PIA /PUMA dust analyzer for the Giotto mission [41]. This allows the integration of new mechanical structures (target and detector components) and a new ion focus optics (ion lens) in an existing vacuum tank.

Simulation of this instrument was performed using the Simion7.0 software using some assumptions on the electrodes and possible voltages. The instrument geometry is defined by the shapes, positions and dimensions of the individual electrodes. Together with the applied voltages the ion optic is determined. As shown in Fig. 3.1 both of the arms have a length of approximately 370 mm. The target segment includes the target, the acceleration grid and two focusing lenses in a cylindrical symmetry along the target normal.

For the calculation of the ion trajectories, it is important to have a well defined plasma generation region. This location is determined by the focus of the dust particle beam or the laser focus. The uncertainty of the focus distance from the symmetry axis is about 0.5 mm in the case of an incident dust particle.

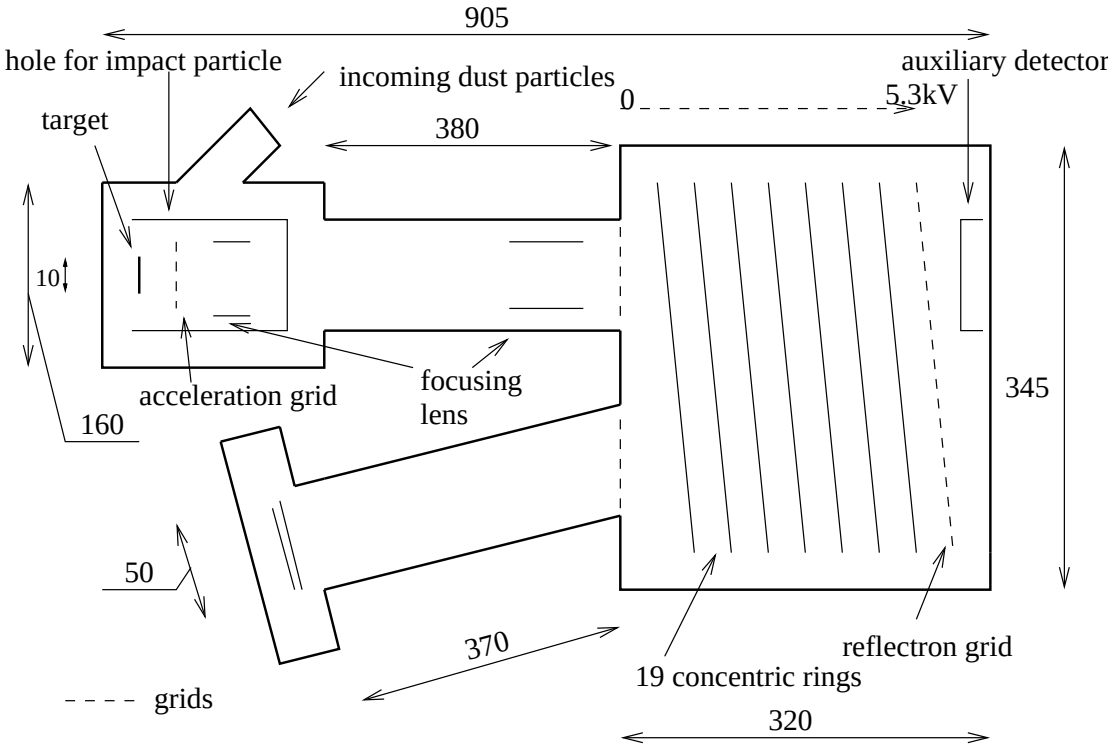

Figure 3.1: Schematic drawing of PIA /PUMA instrument. The instrument has an overall length of about 1.5m. The hypervelocity dust particle will enter the spectrometer at the upper left and impacts on the target. The ions of the impact plasma are accelerated by an electric field applied between the target and the acceleration grid. This acceleration voltage is in the order of 5kV. The ions pass a field free region with two ion lenses before they enter the electrostatic mirror (reflectron). The ions return their direction in the mirror and reach the detector (micro channel plate) after passing a second field free region. The angle between the reflectron and each arm is 7.5 degree.

The target has a sensitive area determined by two factors: First, the ion trajectories must be undisturbed by boundary effects, so the electric field has to be homogeneous in the entire area. Second, the dust impacts generate fragments and ejecta particles which would hit adjacent target, walls, the grids and so on . This effect would lead to the ion generation at area close to the impact location. This has to be avoided in order to detect only the ions from the primary dust particle impact. Therefore, the target area is 10x10 mm and the acceleration region between target and grid is 20 mm.

The first focusing lens can be located either in front of or behind the acceleration grid. In the first case the lens is located in the middle of the acceleration region. In the latter case the lens can be positioned at a distance of 5 mm after the acceleration grid. A close location of the first focusing lens decrease the beam diameter behind the lens. This would increase the beam transmission. The second focusing lens is located right in front of the reflectron entrance.

Between the acceleration grid and the entrance grid of the reflectron the ions movements are affected by the electrostatic fields of the lenses, no further acceleration occurs. Fig. 3.2 shows the configuration of the target section which was used for the SIMION calculations.The mounting

structure for the focusing lens is located above the target region. The mounting structure of the lens is quite close to the target. Therefore, the target and the acceleration grid are inside a metallic cup. This set-up guarantees an undisturbed acceleration region. The cup has a little hole for the laser beam irradiation.

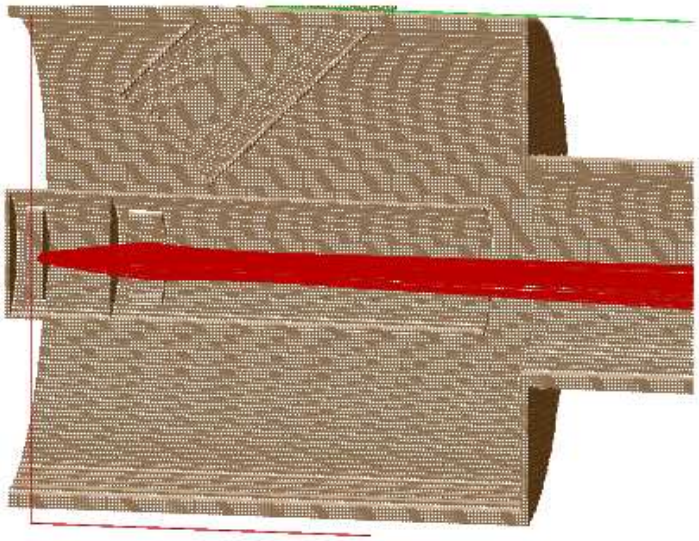

Figure 3.2: Acceleration region of the first arm is used for *SIMION* simulations. The target is surrounded by a metallic shield in order to exclude disturbances of the electric field configuration by the mounting structure of the lens. The first focusing lens is positioned 5 mm just after the acceleration grid. This minimizes the ion beam diameter and leads to a higher transmission.

The reflectron consists of two transparent grids and 19 concentric rings with a uniform spacing. The potential is equally divided to the rings from 0 at the entrance to 5.3 kV at the last grid. The geometry of the reflectron is shown in Fig. 3.3. The reflectron is symmetric about an axis tilted by 7.5 degree to each arm of the spectrometer (inclination). This angle provides the lateral component of the electric field.

The ions entering the reflectron are decelerated and reflected a few centimeters before reaching the last electrode. The counter voltage of 5.3 kV is about 200 V higher than the fastest expected ions (5 kV acceleration and 100 V primary ion energy).

The second arm of the analyzer consists of a 370 mm long drift zone and the detector only. The area from the reflectron to the detector is field free. The ions drift to the detector keeping their velocity unchanged.

The Laboratory model has a sensitive area of about $5cm^2$ and the mass resolution of about 200.

3.1.2 Dustbuster.

The ”Dustbuster” mass analyzer was designed at the California Institute of Technology within the NASA Planetary Instrument Development Program [40]. New design of Dustbuster configu-

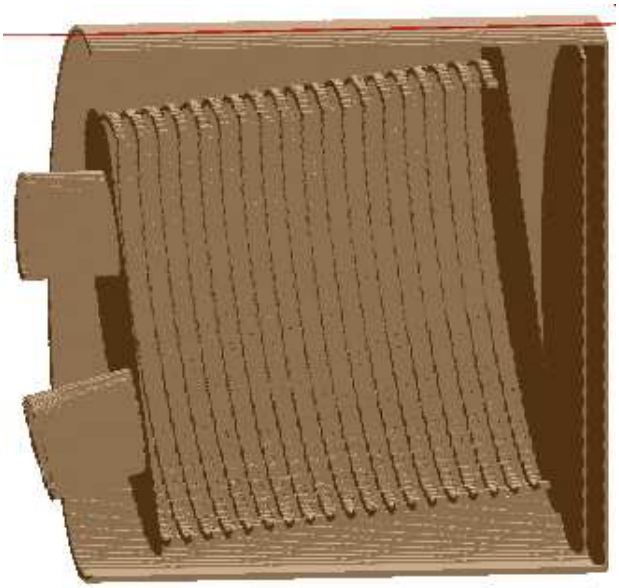

Figure 3.3: The reflectron consists of 19 concentric rings. They are uniformly spaced and the potential applied has values between 0 V (on entry) and 5.3 kV (counter-voltage at last grid).

ration is shown in figure 3.4. The analyzer has a plane target of 65 cm^2 sensitive area. A distance of 10 mm has been used for the acceleration region. There is no field free drift zone between the reflectron and acceleration region. The reflectron consist of one curved grid and five concentric rings with potentials distributed from 0 to 5kV.

The curved grid provides a longitudinal gradient of the electric field and focuses the ions into a hole at the center of the target which constitutes the beginning of a drift tube. The reflectron starts directly outside the acceleration region. The detector is located at the end of the drift tube. Its length is adjusted to provide the best energy compensation. The tube provides additional spatial focusing by an electrostatic lens.

The drift tube confines the amount of ions that can be collected onto the detector. For very narrow beam (2 cm diameter, corresponding to an emission angle of 15 degree and an energy of 50eV)a mass resolution, $\frac{M}{\Delta M}$ (FWHM), of 85 to 300 has been achieved for impacts at different target positions. For a wider beam and more energetic ions the resolution is lower.

In additional simulations the target area has been increased to $0.1m^2$ and the acceleration voltage has been set to 5kV. No appropriate solution have been found to have large sensitive area and high mass resolution.

3.1.3 Swedish configuration

This configuration has been investigated by Håkan Svedhem and Øren [39], two Swedish scientists at ESA/ESTEC. Fig. 3.5 shows the schematics of this configuration. This mass analyzer consists of target-acceleration grid configuration similar to the Dustbuster one, the acceleration

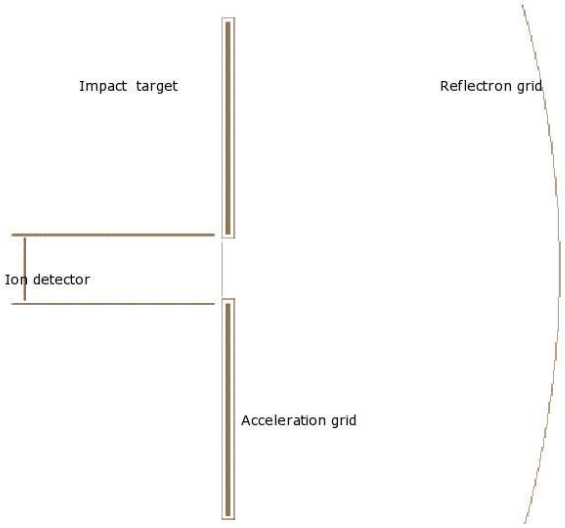

Figure 3.4: Two dimensional view of the Dustbuster mass analyzer. The Dustbuster has some specifi c features. There is no field free region, the ion detector is inside of a tube, providing additional focusing

voltage is 5 kV. Above the acceleration region is a field-free region which is limited by three spherical grids. The reflectron has two stages, defined by 3 grids. The detector is located in the center and has a diameter of 2 cm. Many simulations were performed with this configuration and they showed the following:

- A plane target is preferable over a curved one.
- The potential on the last reflectron grid should be higher by about 100 V than the acceleration voltage. $q \cdot U_{accel} + E_{in} \geq q \cdot U_{refl}$, where q is the ion's equilibrium charge, U_{accel} the acceleration potential, E_{in} is the initial energy of of the ions in eV, U_{refl} is the reflectron potential.
- The analyzer should have cylindrical potential rings with properly adjusted voltages.
- The presence of the middle grids(first and second grids) in the reflectron helps to minimize the size of the analyzer.

The Swedish configuration has the large impact area ($0.1m^2$). The target is at a potential of 5kV. The acceleration distance equals 10 mm. The reflectron has two stages and consists of three grids. All of them have a spherical shape with different radius. Voltages are 0 on the first grid, 3700V on the second grid and 5050 on the third grid. The instrument length is relatively small; only 383 mm.

The dimensions of the reflectron have been chosen using the optimization routines in combination of *SIMION* simulations. Mass resolution of up to 200 (FWHM) have been found, however, only a small part of the ions can be focused onto the target.

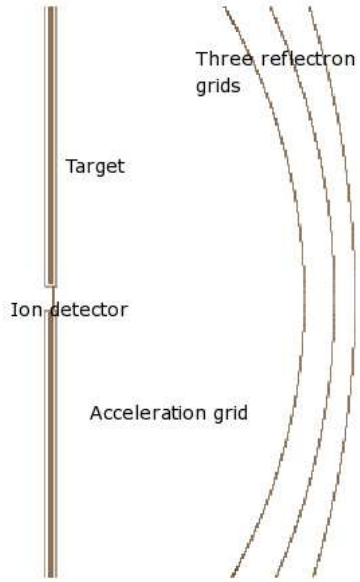

Figure 3.5: Swedish geometry configuration which was investigated at ESA/ESTEC [39]. The two stage reflectron provides a very compact instrument. The reflectrons grids have spherical shapes with different radius of curvatures.

3.1.4 Strong mirror configuration

A configuration employing only a strong mirror reflectron has been studied. A strong mirror reflects ions over a short distance. This configuration can be compared with an optical mirror. No energy focusing is provided by this configuration. Such configuration is shown in figure 3.6 . The configuration consists of a plane target of $0.1m^2$. Above the target is a 0 V potential grid. The potential on the target is +5kV. A distance between target and 0 potential grid is 5mm. Ion acceleration by the electric field happens only within this very short gap.

The reflectron consists of grids located close to each other at a distance of 10 mm. The rest of the analyzer is a field free region. This reflectron acts as a usual optical mirror. This configuration possess a good spatial focusing ability but only very small energy compensation and hence the time resolution and mass resolution are small too.

The possibility of delay line detector anode was studied: ions with different time-of-flights (due to varying emission angles) arrive at the detector at different positions. Therefore, the application of a position-sensitive detector with delay lines was considered. Such an implementation could significantly increase the mass resolution of the analyzer for impacts with a given impact position. However, for impacts at different radial positions the delay lines need to be adjusted differently in order to provide maximum mass resolution.

An alternative way to improve the mass resolution is to shape the detector in a cone. The similarities to light optics show that ions emitted at a given angle with respect to the target normal hit the detector in an ellipse. Again one can apply a concentric delay anode system. An electric signal will be delayed with a dependence on the radial distance. However, this has the

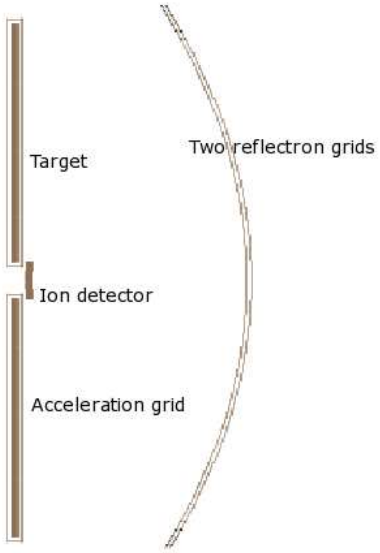

Figure 3.6: Strong mirror configuration. The length of the acceleration region and the reflectron are very small, only 5 an 10 mm, respectively. The reflectron behaves similar to an optical mirror, namely providing a center focus. The detector is cone shaped (see text for further discussions)

.

same shortcomings as the flat concentric ring detector above, therefore, this configuration is not considered any further.

The considered configurations of the dust analyzer have the reflectron implemented. Three of them have high mass resolution. It means the energy compensation works quite well. Nevertheless they all have some disadvantages and require improvements. The final version of new large area mass analyzer is discussed in chapters 4,5.

In this chapter different analyzer configurations with reflectron were discussed. In proceeding section I will discuss elements of designs such as trajectory simulation methods, choice of ion detector and whether a detector forms a shape of spectral lines.

3.2 Modeling and components of a mass analyzer

The characteristics of the mass analyzer have already been mentioned. However there is a need to describe the simulations performed. What assumptions were made to the ions, why the chosen voltages are optimal and show the simulated trajectories and simulated spectra. In connection it should be noted that in the simulations the ion detector is a thin line. No physical processes were considered. Indeed the ion detector can define a shape of spectra lines and their dispersion. In this section I will discuss requirements and the choice for the ion detector.

3.2.1 Ion trajectory simulations using *SIMION*

Results of simulation can be very different because of different initial ion conditions and simulation method. Therefore in this section I discuss the initial conditions of the ions and simulation environments.

For the simulations the Simion 7.0 software package used was developed by Idaho National Laboratory[42]. The first step in *SIMION* spectrometer simulations is to describe the electrode geometry. For this PIA-PUMA type analyzer the electrode geometry has a precision of 1 mm that should be enough because most of the important regions have dimensions ten times more. For example acceleration distance is 20mm. When the geometry file is ready and loaded *SIMION* calculates and assigns a potential for each point in a three-dimension space with the step of 1mm
.

The next step is to describe the ions at where they start near the target and values of initial conditions. The Values are assigned to the ion *energy* , the two ion emission angles *azimuth* and *elevation* and the ion *mass* and spatial coordinates x,y,z. Ion energies were assigned to 0-50 eV range. The angles lie between -90 and +90 degrees. Each parameter of the uniformly distributed ions was generated using a random generator. These distributions are shown in Fig. 3.7. Then

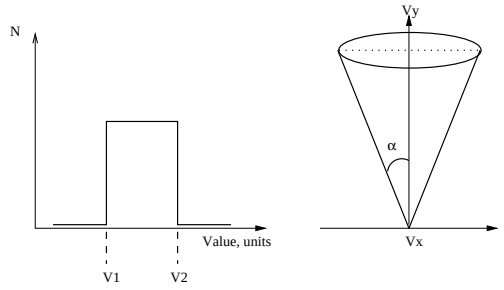

Figure 3.7: Energy (left) and angular distribution (right) of the ions at the target (initial conditions). The *SIMION* simulation requires a file which describes the ions (start position, emission angle and energy). In the simulations usually 1000 ion trajectories were calculated. Each ion has its own initial parameters. The values of for the ion energy and emission angle were created using a random generator and a uniform distribution of ions.

when letting the ions fly the program calculates and visualizes the paths of the ions through the analyzer. The software package writes an output to a file which contains the time-of-flight, the ion mass, the field gradients and some other values.

In order to define the mass resolution, ions of the same mass are assigned to groups and the time-of-flight distribution of each group is approximated by a Gaussian distribution. The peak width is characterized by the Full Width at Half of Maximum (*FWHM*) and it is defined as $\cdot 2.32\sigma$ where σ is a parameter of Gaussian distribution;

$$f(x)dx = \frac{1}{\sigma\sqrt{2\pi}} e^{-\frac{(x-X)^2}{2\sigma^2}} dx \tag{3.1}$$

where X is a mean value of x.

All processes including the geometry file preparation, assigning initial conditions and data treatment was automatic using following schema. The SIMION software takes care of simulation routines. In order to analyze the output data another MATLAB software is used that makes the entire simulation process more efficient. The flow chart diagram in Fig. 3.8 illustrates the process. The software *Matlab* 5.3 is used in order to create the ion geometry configuration files

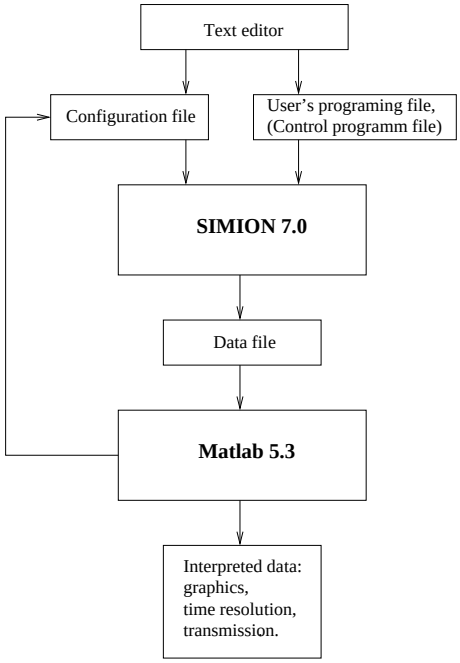

Figure 3.8: Flow chart of SIMION geometry creation. *MATLAB* creates a geometry file and ion source file using loops. Then *SIMION* simulates the geometry, performs the calculation and produces an output text file. Finally, *MATLAB* processes and visualizes the data.

and the ion input specifications. Then the *SIMION* 7.0 software reads these data and creates their own file describing the geometry and potential distribution. *SIMION* visualizes trajectories and produces the output file containing the flight time data. Then again *MATLAB* processes and visualizes these data. The results of this intensive calculation are the values of the mass resolution and the ion transmission.

Fig. 3.9 shows simulation of the laboratory model. The reflectron has 7.5 degree inclination both to the first drift region and to the second drift region. In order to show the analyzer structure two cross-sections were made. One can see the ion trajectories as continuous color lines. Ions start near the target with different initial conditions then are accelerated and focused on the ion detector using a reflectron. The lenses help to focus the ions to the reflectron where ion energies are compensated to have approximately equal flight time to the ion detector.

When reflected the ions fly to the ion detector. No additional focusing is done after the reflectron. All of the ions are focused on the ion detector. Usually the flight of one ion mass was simulated which is of 200 atomic mass units.

In practice it could be difficult to define position of impact. So the mass resolution was

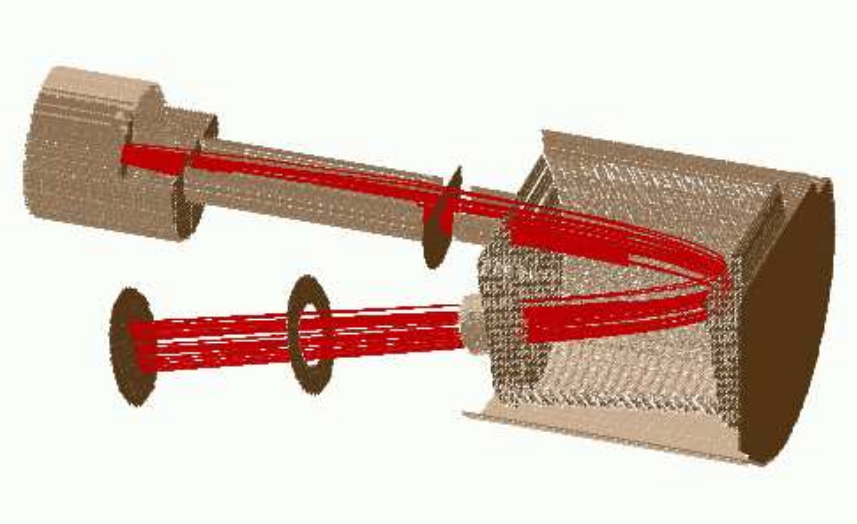

Figure 3.9: The ”High Resolution Mass Analyzer” in the *SIMION* environment. Red lines indicate ions trajectories. Almost all of the ions are collected onto the detector

defined for two cases. One case is if the ions start flying from a point at the center of the target(point source). Another case is if the ions start flying at different target positions(extended source). Spectrometer simulations show the resolution $\frac{m}{\Delta m} = 200$ for the point source and $\frac{m}{\Delta m} = 121$ for 10 mm diameter source.

The flight time distribution for the mass 200 and the corresponding time resolution is shown in figure 3.10. This is the case when the ions are emitted from one point on the target. In fact different detector area is required for these two cases. The Figure 3.11 shows the positions of the ions in the detector plane. Each point corresponds to one ion hitting the detector. In the case of a point source the area at the detector required is less than 10mm. In contrary, an ion source with a diameter of 10mm at the target needs a detector with a radius of 56 mm. It means when the impact position is not known exactly ($\pm 0.5cm$) the instrument requires a sensitive detector with a radius of 28 mm. Because of impact uncertainty the mass resolution and the transmission were measured at different points within 5mm radius. The smallest focus as well as highest mass resolution is for impacts on the target center.

Simulation results for different starting points at the target are shown in Tab. 3.2. The mass resolution of 221.7 can be explained in the situation where part of the ions are absorbed be the elements of the spectrometer and consequently Δm is less. It should be noted here that it is better to have the ion's hits uniformly distributed over the detector area since the count rate is quite high and each MCP channnel has to detect just one ion without loosing its multiplication.

An important improvement was made to the target. The distance between the target and acceleration grid is increased so the formation of ion cloud occurs in the acceleration region. The target holder should allow for a sample rotation in order to expose different sample surfaces. The target can be hit either by a dust particle of the accelerator or by a short laser pulse. In latter case it could require a special design for the target region if the focusing system of the laser set-up is inside the spectrometer vessel. The target is encapsulated into the metallic cup in order

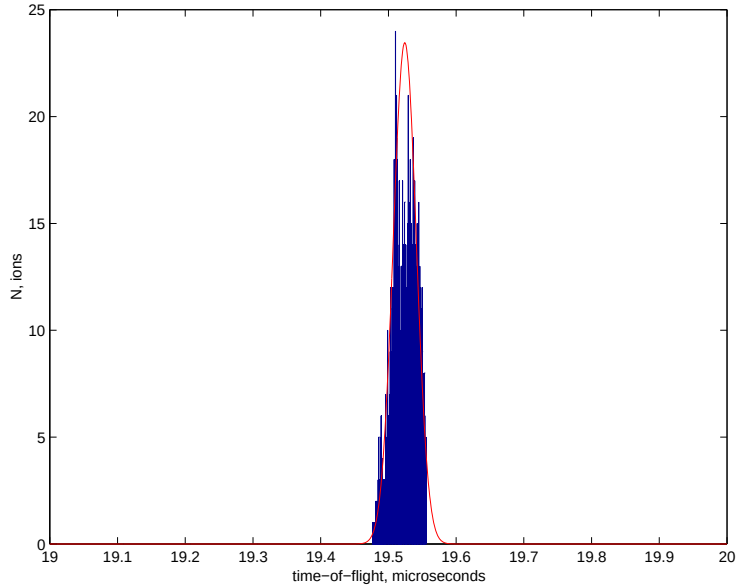

Figure 3.10: Mass resolution of the point source (ions start at x=y=0 at the target).

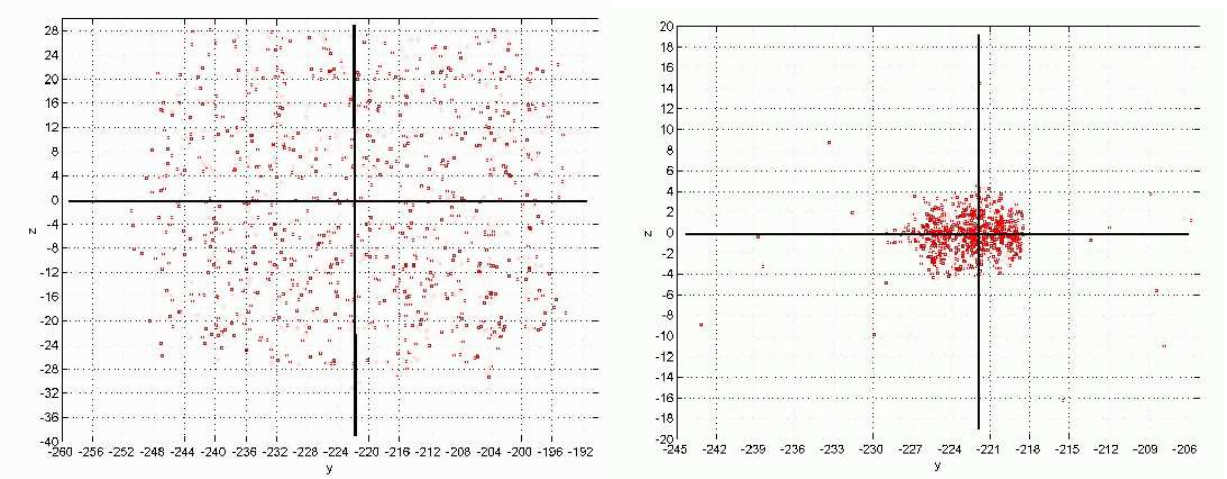

Figure 3.11: Spatial distribution of ions hitting the detector. The red points indicate the positions of ions in mm arriving at the MCP detector surface. For the extended source (left) and for a point source (right).This shows the ion distribution at the detector plane. Each point represents a single ion.

n	z,mm	y,mm	transmission, %	beam diameter, at the detector plane, mm	shift, mm	mass resolution, $\frac{m}{\Delta m}$
1	0	0	89,5	8	z=0, y=-1	200,3
2	0	-5	86.4	8	z=0, y=25	182
3	0	5	84.8	8	z=0, y=-26	221,7
4	-5	0	88.2	8	z=27, y=-1	197.6
5	5	0	88.3	8	z=-27, y=-1	189,9
6	all	all	87.9	56	z=-1, y=-1	121,9

Table 3.2: The result of *SIMION* simulations. The spectrometer has an axial symmetry. If the starting ion position is not on the symmetry axis the mass resolution and transmission are low. This table shows the spectrometers parameters with the dependence of the emission point on the target. The last line shows the parameters for an extended ion source with a starting position of a 5 mm radius.

to exclude disturbances of the electric field caused by the focusing elements of the laser. In the cup there is a small hole for a laser beam.

The laser pulse has a duration of 6*ns* that is comparable with interaction time of a dust particle and a solid target. An energy pulse of $\leq 600\mu J$ is generated by triple Nd:YAG with a wavelength of 355*nm*. The laser is a diode-pumped Nd:YAG laser with a Gaussian beam profile in order to achieve a good laser focus. The optical system has a focal length of 80 mm.

In most of this chapter only the mass resolution of the instrument was discussed. Another important feature is the ion transmission. The spectrometer transmission is defined as the ratio of the number of the ions reaching the detector to the number of ions starting at the target. When starting from the target the ions are accelerated and fly through the system of electrodes. Some of the ions having largest lateral velocity component leave the ion beam and hit the analyzer wall, not the ion detector. Several lenses were used to confine the ion beam and focus it on the detector. Optimal voltages for these lenses were found using the voltage permutation during SIMION simulations.

3.2.2 Voltages

The voltages on the focusing lenses were determined using the control programming language of Simion software. The routine written calculates the ion transmission with respect to the lens voltage. The analyzer has two lenses. One is in the target volume. Another one is in front of the reflectron. The target voltage is selected to be +5kV in order to make the ion beam narrower so it becomes more easy to focus the ions. This also ensures a high electric field for the acceleration region. The acceleration grid is grounded. The voltages on the reflectron are uniformly distributed through 19 rings from 0 on the entrance grid to +5300 V on the last ring. Each part of the spectrometer has a cylindrical symmetry. The symmetry axis of the reflectron is inclined to the symmetry axis of the drift tubes by an angle of 7.5 degrees with respect to each arm. The electric field strength inside of the reflectron is constant. Because of the reflectron

The target voltage is 5,0 kV.
The acceleration grid is 0.0 V.
The voltage at lens 1 is 3,0 kV.
The voltage at lens 2 is 1,3 kV.
The reflectron voltage grows linearly from 0 V on first grid through the 19 rings to 5,3 kV on the last reflection grid.
The voltage at the detector plane is set to 0 V.

Table 3.3: The table shows voltages of the analyzer

inclination a component E_y appear and the ions change their flight direction and move to the second drift region and hence to the ion detector. If an ion has an energy of more than $5300eV$ it flies through the last ring and deposits its energy on an auxiliary detector located at the end of the reflectron tube.

The two field free regions are separated by grounded potential grids from the environment. The micro-channel plate detector has a -2kV potential at the front side. The anode has a potential of below +100 V. Basic voltages of the analyzer are shown in the table 3.2.2 The target voltage has to be high enough in order to provide high transmission and low enough in order to avoid sparking. Voltage on the reflectron has to be chosen from the following considerations: after an impact an accelerating ion possesses energy equal to $E_{acceler} + E_{init}$, where $E_{acceler}$ is the energy got from accelerating field and E_{init} is the energy of initial conditions. 30eV was chosen for E_{init} the voltage on the last reflectron ring is 5.3kV. This assumes that only the particles having energy $E < 300eV$ will be reflected by the reflectron the others will fly through.

The voltage on the lenses is chosen under the conditions of having maximums of ion transmission using so-called user programming files.

The determined voltages were chosen for further simulation within the Simion environment. In these simulations the detector was assumed as a thin plane for simplicity and it had no influence on the shape of the spectra. If such considerations are fair, what should we choose for the ion detector?

3.2.3 The ion detector

There are a number of different detector kinds, such as gas chamber, silicon detector, photomultiplier, channeltron and so on. The ion detector should be compact and light. It should be able to detect heavy ions of 1-5keV energies. The ion detector for the analyzer has to work at a high count ratio. The total number of ions can exceed the value of 10^6 for a single event. One can propose two options; a micro-channel plates(MCP) and a micro-sphere plate detectors. Both detectors are compact and light electron multipliers. They both can work with the high count rate.

The MCP detector consists of 10^6 channels per cm^2. Assuming uniform spatial ion distribution through the detector area, each incoming ion will be detected in one single channel. The recovering time of 1ms plays no role, since expect another dust particle after 1s and hence an-

detector	time resolution , ns	gain	Voltage, kV	spatial resolution, ln/mm*
micro-channel plate	0.7	10^6	2	16
microsphere plate	0.8	10^7	3.5	2

Table 3.4: Compared characteristics of micro-channel plates and microsphere plates detectors.

The effective diameter is 50mm.
The individual channel diameter is 12μm.
The bias angle of the channels are 8 degree.
The bias voltage is 700-1400 V for each plate.
The thickness is in the range of one mm.
The amplification is in the order of $5 \cdot 10^3$.
The time resolution is better than 700ps.

Table 3.5: Parameters of microchannel plate detector

other electron avalanche appears later, when channel amplification was recovered. 3.4 compares the parameters of these detectors. As can be seen from the table they both have very similar parameters. *lines/mm.

The microsphere plate is a very new detector, consisting of small spheres and can be used both for high count rate detection and for spatial detection.

The choice was made to use MCP because of some problem of MSP manufacturing. The MCP detector also has the proven advantage of long life which is of great importance for in-situ experiments. For example, the micro-channel plate detector loses its amplification after several years. Even so, in the last years some novel developments of the micro-channel plate detector were made in order to increase its long term stability [43]. The parameters of the micro-channel plates detector [44] are listed in the table 3.5

The fig. 3.12 explains principles of operation for the microchanel plate detector. The MCP consists of millions of individual channels, each of which work as an electron amplifier. If an incoming ion, or an electron hit the surface of MCP channel, it releases two-three electrons. These are accelerated and release other electrons when traveling through an MCP channel . The total charge multiplication reaches a value of 10^3 for one plate and $10^6 - 10^7$ for chevron configuration.

The detector area is large and has a diameter of about 80 mm. A large detector area is required due to the fact that the ions have a broad distribution in emission angles with respect to the target. This translates into a wide focus at the detector plane. Applying a phosphor screen as a detector anode provides the possibility to make a visual image of the spatial ion distribution at the detector plane. The phosphor screen can be observed through a window in the detector flange. This detector is provided by the company El-mul corp under the product number RE050JPW.

Generally, the high resolution analyzer uses three detectors. First is the impact target. Second is the ion detector. There is also an auxiliary ion detector at the ”bottom” of the reflectron which is a simple copper plate. If the ions have an initial energy above 300eV, exceeding the counter-voltage of the reflectron(5.3kV) minus the accelerating voltage(5kV), they can pass through the

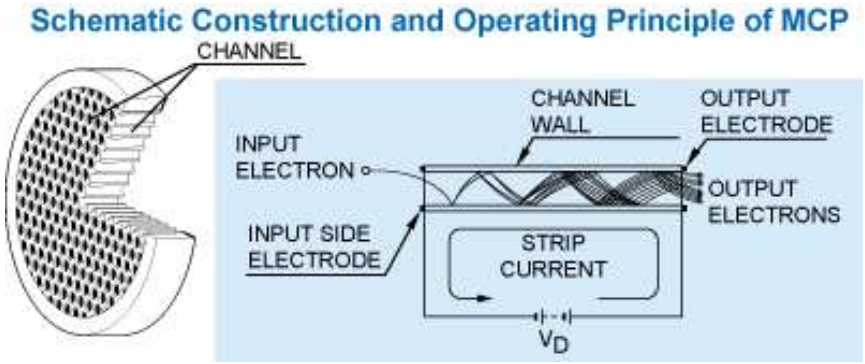

Figure 3.12: The micro-channel plate detector. The detector is an electron multiplier. Its amplification is 10^3 for a single plate. The micro-channel plate consist of millions of single channels. Each of those is a small detector. Because of the small size of single channels, the time resolution is very high and can reach the value of 700 ps.

last grid and hit this detector located just after the last reflectron grid.

Thus the ion detector for the laboratory model was chosen as a microchannel plate detector and some words should be said about influence of an MCP detector on the shape of spectral lines . Eventually, one can mention two factors with regards to the lines shape. One factor is time resolution of an ion detector. Another factor is how well each group of ions separated from others at the first moment of expanding plasma.

3.2.4 Energy deposition at the ion detector

The factor of the expanding plasma is due to the impact phenomena, and should be explained from that point of view. Taking to consideration the detector, one can estimate its influence on lines shapes. The ions are accelerated in the acceleration region up to +5 keV and are reflected to the detector. The value of the charge Q at the detector output and the time resolution FWHM [1] can be estimated for a micro-channel plate detector.

Each impacting ion transfers its energy E to the surface material of the detector. Only a part of this energy is responsible for an ionization $\int_l \frac{dE_{ion}}{dX} dl$. This energy deposition is proportional to released electrons. These electrons have a charge q, and the total charge proportional to a number of electrons N released:

$$Q = qN = \frac{q \int_l \frac{dE_{ion}}{dX} dl}{I_{ion}} \tag{3.2}$$

Where I_{ion} is ionization potential for the detector material, and the l is the ion trajectory. The micro-channel plate detector is an electron multiplier. Its amplification can be characterized by a Gaussian distribution with a mean value of 10^6 and $\sigma = FWHM/2.32$. [2].

[1] Full Width at the Half of Maximum, a usual procedure is to fi t the Gaussian distribution to the experimental one. Then the set-up properties can be described by Gaussian value σ. The σ relates to FWHM as $sigma \cdot 2.32 = FWHM$

[2] The value of FWHM is given in HAMAMATSU product catalog [44]

$\left(\frac{dE_{ion}}{dx}\right)$ can be defined by the tabulated data or its computer implementation(cite?). Each ion hit the detector produces a voltage pulse U(t) in the detector circuit, of the shape ;

$$U_i(t) = \frac{Q_i}{C}\frac{e^{-\frac{(t-t_i)^2}{2\sigma^2}}}{\sigma\sqrt{2\pi}}$$

and the total pulse;

$$U(t) = \sum_i \frac{Q_i}{C}\frac{e^{-\frac{(t-t_i)^2}{2\sigma^2}}}{\sigma\sqrt{2\pi}} \tag{3.3}$$

Let us define the case if the initial conditions are equal to 0 or another constant.In this case the flight time of ions will have the same mean value t_0. The voltage pulse can be expressed as

$$U(t) = \frac{e^{-\frac{(t-t_0)^2}{2\sigma^2}}}{\sigma\sqrt{2\pi}}\sum_i \frac{Q_i}{C} \tag{3.4}$$

C is the equivalent capacitance of the detector and electronic circuit. t_0 is a mean time of the flight time. From the measurements it is known that the peak width of the most thin line ^1H is 20ns(FWHM)(see section Measurements). As can be seen from the above equation, the detector deposition into the peak width is significantly smaller. FWHM for a single pulse is about 0.7ns and should also be the same for all ions of the same ion mass. Thus the width of mass lines does not depend on the time resolution of the ion detector and depends on a range of ion initial conditions when using the microchannel plate detector .

Using results of the work described in this chapter, some measurements were done that are described in the proceeding section.

3.3 Measurements

The Heidelberg dust laboratory has a linear mass analyzer and mass analyzer with a reflectron. The linear analyzer is a tube with a flight distance of about 1.4m There is a target in the beginning and the mcp detector in the end of tube. The mass analyzer with a reflectron is the PIA/PUMA prototype(laboratory model). It has a flight base of about 1.5m. The ion detector was the microchannel plate detector.

Some measurements were done using both a linear mass analyzer and mass analyzer with a reflectron for iron dust particles in velocity range v=9-50km/s.

The results got on the linear analyzer were compared with data from the laboratory model of PIA/PUMA analyzer that has a flight distance about 1.5m. The linear mass analyzer shows mass resolution of about 140 if using the silver target and the iron dust particles. The figures 3.13 and 3.14 show the mass spectra of the linear mass analyzer and the reflectron type of the analyzer. Both instrument use a silver target(the natural silver for the linear analyzer and the black silver for the laboratory) and an iron projectile. For the first spectrum the projectile velocity is 11.9 km/s. For second case the velocity of the projectile is 10.6km/s.

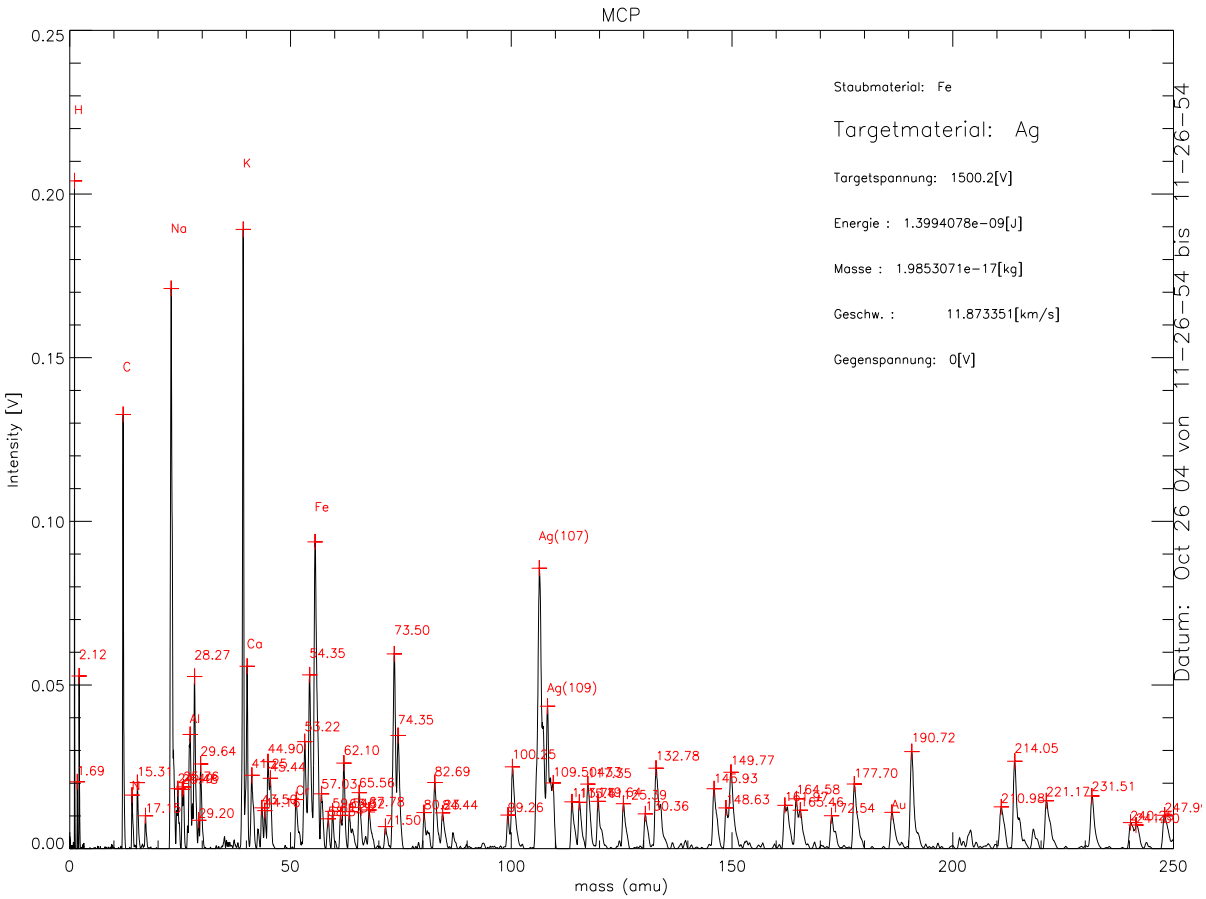

Figure 3.13: Mass spectrum of linear analyzer. The target is a silver. The projectile is an iron particle.(Anna Mocker)

The mass resolution of the laboratory model significantly exceeded the mass resolution of the linear mass analyzer and reached 260. This means that the laboratory model allows us to separates the main lines of most elements in cosmic space. The simulation process was an automatic one(creation of geometries and analisys of the data), that significantly simplified the task of finding the optimal configuration. The microchannel detector, which is a compact electron multiplier with high amplification and can work at high count rate, was chosen as the ion detector.

Another task is to compare the results of computer simulation to the results got from the measurements. At first one need to look at the data and define the ion species. Then specifications of ion species can be introduced into Simion simulations and the resulting mass spectrua can be compared with the measured ones. It is assumed, that only silver peaked will be compared, since if the silver peak is resolved, than the others, having a lower mass, are resolved too.

As the laboratory model was used for an investigations of the impact process one use these data. A solid target of the mass analyzer was impacted both by the dust-like particles and by the laser shot.

Here I present the results that were got using the dust accelerator. Most of the experiments

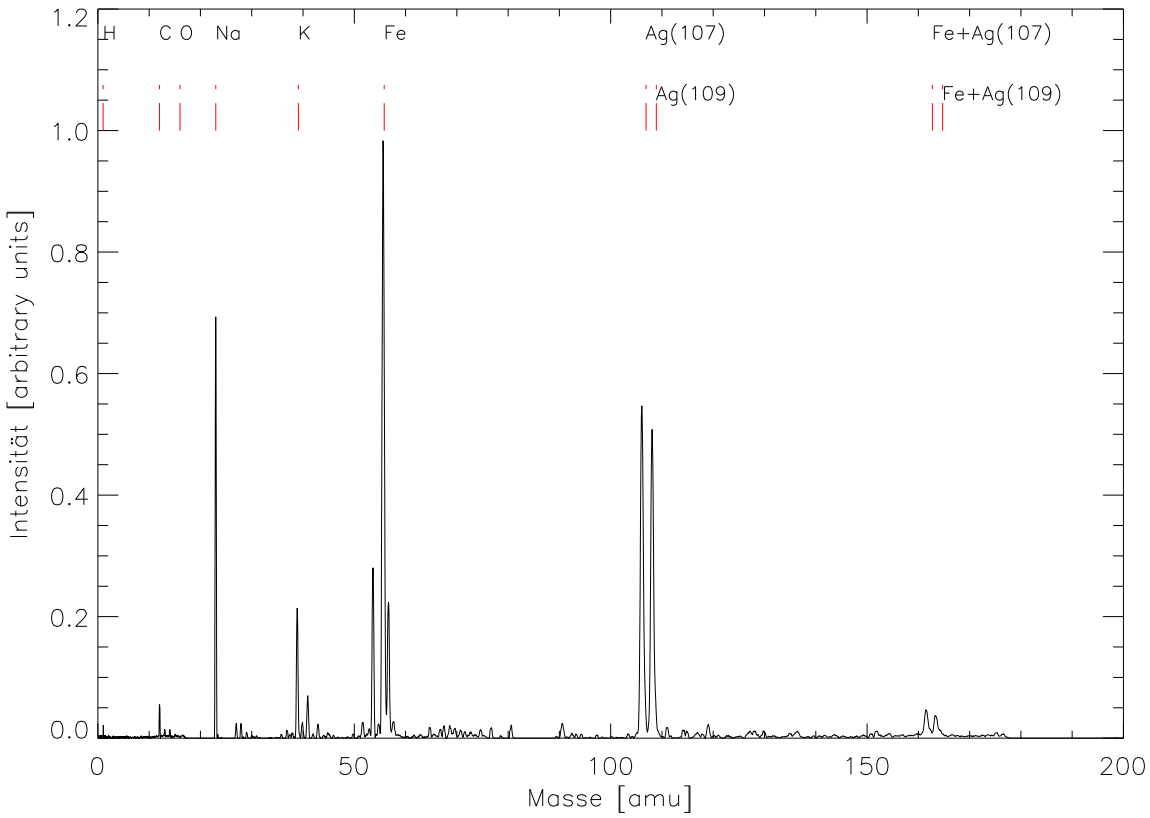

Figure 3.14: Mass spectrum of mass analyzer with a reflectron. The target was made from silver. The projectile is an iron. The red lines give the main numbers(a.m.u) or element identification(Anna Mocker)

have been conducted with a Silver target(so-called black Silver). The target was mounted to a movable support in order to change a new undamaged position of the target for each shot. The iron particles were used as projectiles. The velocity changes in a range of 9-15km/s. Actually, three cases are presented here. The first one is for the particle's velocity of 9.5km/s, the second one for the velocity of 10.6km/s and the third one for the velocity of 15.0km/s. In the beginning some changes that were made to the laboratory model are disscused.

Since all available data was gathered with a 1kV acceleration voltage, the same voltage was used for the measurement. It means that the target had 1kV potential and the acceleration grid was grounded. The slightly increased potential was chosen for the reflectron. It was on 1.1kV potential. All ions having an initial energy less than 100eV were reflected. As the ion detector, the chevron configuration of microchannel plates (MCP) detector was used. The MCP detector was under the potential of -3,5kV. Instead of two lenses, one was used under potential of 420 V.

The target is under positive potential in respect to the acceleration grid and collects electrons released during the impact. From the collected electron charge Q_e, one can roughly estimate the released charge, which is a combination of ionized target material and the ionized projectile material.

The time-of-flight spectrum achieved by the laboratory model is shown on figure 3.15. The projectile is *Fe* iron particle, particle mass is $1.88 * 10^{-17} kg$ and acceleration velocity is 9.5km/s. The spectrum shows distinguishable features of the projectile *Fe*, the target material ^{109}Ag and

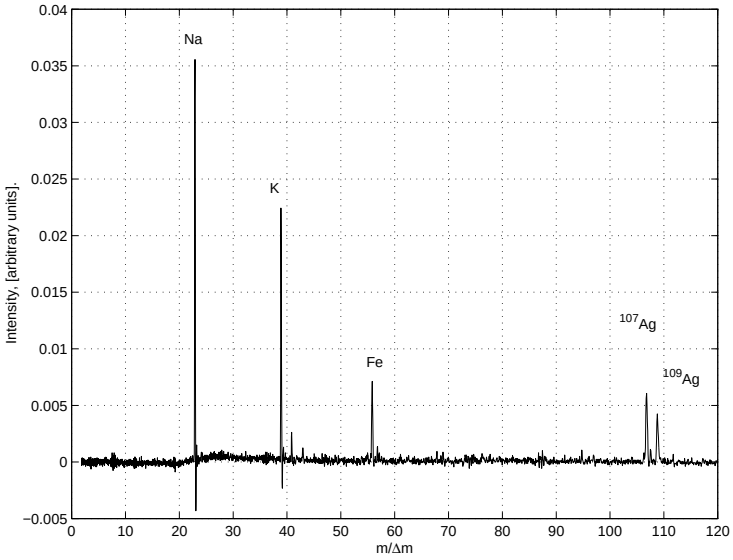

Figure 3.15: Time-of-flight spectrum of the ejected ions. The target material is a silver. The projectile is a particle *Fe* with velocity of 9.5km/s.

^{107}Ag those have abundances of 51.83 percent and 48.17 percent consequently. The other peaks correspond to the target contaminations that always exist. Those are ^{23}Na and ^{39}K. The mass resolution estimated from the silver peak is 176.

The next figure 3.16 shows the mass spectrum for a particle velocity of 10.6km/s. The same elements ^{23}Na and ^{39}K, *Fe*, ^{109}Ag, ^{107}Ag exist in this spectrum. However the ratio between the

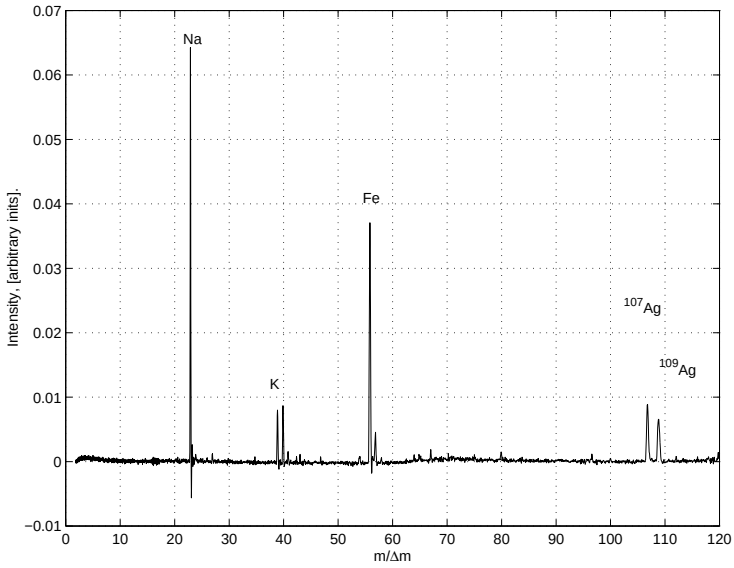

Figure 3.16: Time-of-flight spectrum of the ejected ions. The projectile is a *Fe* particle with velocity of 10.6km/s.

peeks is different. The ^{23}Na peak is the same. For the ^{39}K, an intensity is three times lower than for velocity of 9.5km/s. The intensity of the *Fe* peak is 3 times higher. The intensities of ^{107}Ag and ^{109}Ag are a little bit higher as well.

The figure 3.17 shows spectrum of the *Fe* particle with velocity of 15km/s. The ^{1}H and ^{12}C peaks appear in the spectrum. The ^{23}Na peak has the same intensity. The intensity of ^{39}K is lower than at a velocity of 10.6 km/s. The intensity of the projectile *Fe* peak is higher, and both ^{107}Ag and ^{109}Ag peaks show a significant grow.

The spectra discussed show the features of the target material, the projectial material and the impurities such as; hydrogen, sodium, and kalium. One can reproduce these features in Simion modeling using ion descriptions. The intensities of the peaks supposed to be not exact as it plays no significant role. The mass resolution will be fit using assumption for the ion energy and the ion emission angle. One of the simulated spectra is shown in fig. 3.18.

All ion species were introduced into the ion file. The intensities are different because of different ion amounts introduced. The peak width relates to the initial conditions of the ion species.For this particular case the energy was uniformly distributed over 0-50eV range. The angle was also uniformly distributed over the range -15, +15 degree range. For these initial ion conditions the mass resolution $m/\Delta m$ becomes 225 for the ^{107}Ag silver line. This spectrum was compared to the fig. 3.17 which shows the mass resolution $m/\Delta m$=267.5 for the ^{107}Ag silver line.

From the simulations of the ions spectra one can conclude that the angular distribution have the most big effect on the mass resolution. In order to match the measured spectra the initial angle range should be within $\pm$(0-15) degree, due to normal of the impact target. The energy should be less than 30eV.

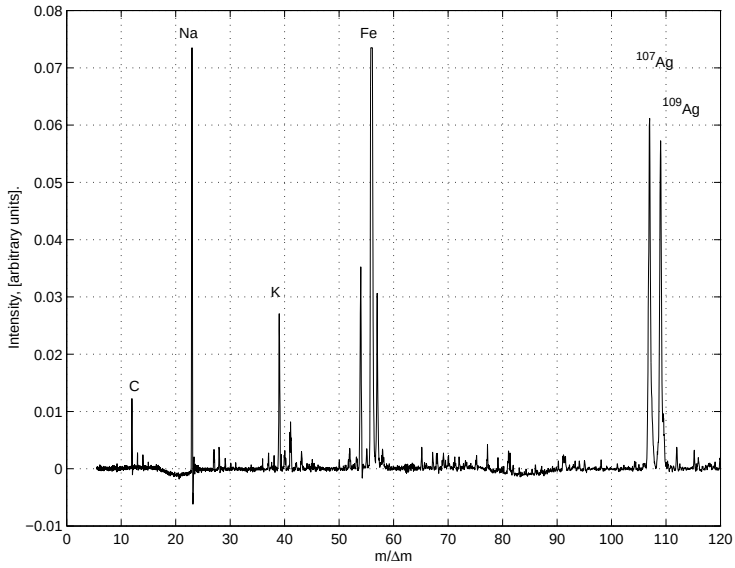

Figure 3.17: Time-of-flight spectrum of the ejected ions. The projectile is a *Fe* particle with velocity of 15.0km/s.

The main task of this chapter was to compare results of simulations to the measurements. When comparing, one can see that the results of simulations are very similar to the measured results. Therefore one is recommended to apply the modeling of Simion7.0 to the large area mass analyzer. This is discussed in the next chapter.

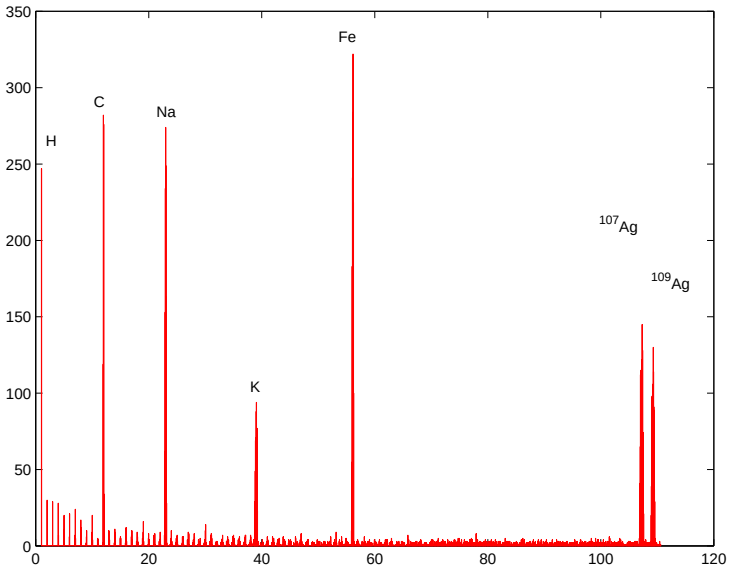

Figure 3.18: Simulated time-of-flight spectrum of the ejected ions. All ion species were introduced into the ion file. The intensities of the peaks were chosen arbitrary. The noise was introduced using a random generator. The mass resolution $m/\Delta m$ is 225 for the ^{107}Ag silver peak. All the ions have the energy of initial conditions from 0 to 10eV and the emission angle varies from -15 to +15 degree

Chapter 4

The Large Area Mass Analyzer (LAMA)

The LAMA is a time-of-flight spectrometer which fulfills these two main requirements:
1. the instrument shall have a sensitive area of at least $0.1m^2$, and
2. the instrument shall provide composition analysis of each impacting grain with a mass resolution $\frac{M}{\Delta M} \geq 100$.

The dust instrument must have a large sensitive impact area, because of the low dust particle flux in space. The smaller impact areas of previous mass analyzer instruments were acceptable, because these instruments were optimized for the high dust fluxes near comets or in Saturn's ring system.

The high mass resolution is required in order to separate elemental ions up to mass 100, which covers the most relevant elements expected in cosmic dust.

There are further requirements that should be considered by the design of LAMA in this PhD work:
3. The acceleration distance for ions shall be 50 mm, and the acceleration voltage shall be 5 kV, and
4. the reflectron must provide both time and spatial focusing.

The acceleration region for ions is several times bigger than that for CDA (3 mm) and CIDA (10 mm). Thereby, the effect of shielding in the dense initial impact plasma cloud will be reduced, because the plasma cloud is allowed to expand into a much larger volume within which the ions are separated from the electrons by the electric field. This should provide high resolution mass spectra also for impacts of big and fast particles which generate large number of ions.

Typical ion detectors (multipliers or microchannelplates) have a radius of up to 25 and 35 mm, respectively. Such an ion detector should collect a large fraction of the ions generated upon dust impact, therefore, the ions must be focused onto the smallest detector area possible.

This chapter describes the design of the large area mass analyzer(LAMA). The analyzer configuration found, satisfies the mentioned requirements, and the parameters of this configuration are described below.

The new dust sensor devoted to the Dune mission has to include a chemical analyzer and a sensor defining the particles trajectory, mass and velocity(Trajectory sensor). The LAMA configuration was adjusted to combine these two instruments.

In the beginning, a theoretical approach for an ion trajectory determination and an equation of

motion in an electric field are considered. In the case of a simple field, this allows us to optimize the mass analyzer.

Using numerical methods one can find values of an electric field in a complex analyzer geometry. A method for calculating the electric field used in Simion software will be considered here as well.

The configuration of mass analyzer is a complex one, and contains a large number of parameters to calculate. The parameter optimization is easier to achieve using different methods of computer model programming.

4.1 The optimal configuration of the time-of-flight analyzer

This section discusses th method finding an optimal configuration of electric field for the time-of-flight mass analyzer with a reflectron. The problem is finding the potential distribution which provides the best time resolution and the best spatial focusing. One can find the solution using both analytical or numerical methods. Unfortunately, even for a simple configuration, it is very difficult to find the analytical solution. The real electric field contains disturbances. Because of that, the time resolution and spatial focusing can be different from that of the calculated ideal case. However, the analytical solution can be useful to define the direction of the investigations, and the preferred geometry of the electrodes (hyperbolic, parabolic or planar).

4.1.1 An analytical solution of the electric potential

The successful application of time-of-flight spectrometry for a mass and energy determination have led to a wide use. The time-of-flight methods became accessible after new electronics was developed, allowing measurements of time steps of $10^{-6} - 10^{-9} s$. The ion mass measurement is done by a measurement of the flight distance and the flight time. Time-of-flight mass spectrometry is basically dealing with the measurement of the mass-to-charge ratio(m/z) of the ion.

$$E = \frac{mv^2}{2} \tag{4.1}$$

$$t = S\sqrt{\frac{m}{2E}} = S\sqrt{\frac{m}{2qU}}\,, \tag{4.2}$$

E is the kinetic energy, m is the mass, v is the velocity of the ion, t is the flight time, S is flight distance, q charge of the ion and U is acceleration potential. The electrode potential U and a charge of the ion q are constant, thus a mass m is unambiguously defined by a flight time t. The equation of motion is built on the basis of Newton's law

$$m\ddot{x} = F \tag{4.3}$$

The force F acting on a charged particle with a charge q moving with velocity v in electromagnetic field E and B is

$$\vec{F} = q(\vec{E} + \vec{v} \times \vec{B}) \tag{4.4}$$

A purely electric field will be applied in the instrument.

$$m\ddot{x} = qE \tag{4.5}$$

The electric field $\vec{E}$ is defined by Laplace's equation.

$$\text{div grad } u = 0 \tag{4.6}$$

The analyzer will have a cylindrical symmetry therefore it is convenient to use cylindrical coordinates

$$\begin{aligned} x &= r\,cos\,\alpha \\ y &= r\,sin\,\alpha \\ z &= z \end{aligned}$$

In cylindrical coordinates the Laplace's equation becomes

$$\frac{1}{r}\frac{\partial}{\partial r}\left(r\frac{\partial u}{\partial r}\right) + \frac{1}{r^2}\frac{\partial^2 u}{\partial \alpha^2} + \frac{\partial^2 u}{\partial z^2} = 0 \tag{4.7}$$

Since the potential u is a periodic function of α with period 2π, it can be expressed as the expansion in a Fourier series:

$$u(r,\alpha,z) = \sum_{m=0}^{\infty} [a_m(r,z)cos(m\alpha) + b_m(r,z)sin(m\alpha)] \tag{4.8}$$

This expression yields in the case of axial symmetry [45]

$$u(r,z) = \sum_{k=0}^{\infty} \frac{(-1)^k U^{(2k)}(z)}{(k!)^2}\left(\frac{r}{2}\right)^2 = U(z) - U''r^2/4 - U^{IV}(z)r^4/64 - U^{VI}(z)r^6/3204 \pm \ldots \tag{4.9}$$

Where $U(z)$ is potential distribution along the axis of rotational symmetry z. The potential distribution $U(z)$ along z fully defines the potential distribution $U(r,z)$. A possible problem is to find the potential distribution u(0,z) along the axis z . Recently E. Grün proposed the solution for the large area mass analyzer. The solution is found using the *SIMION* ion optics software. In order to check whether it is possible to improve the configuration the potential distribution along z axis was measured. The potential distribution u(r,z) was found using the equation 5.1. The potential distribution along the z axis (r=0) is taken from the large area mass analyzer simulated by *SIMION 7.0* software.
If the distribution of the potential is known an ion trajectory equation become

$$\frac{\partial^2 r}{\partial z^2} = \frac{1 + r'^2}{2(u - u_0)}\left(\frac{\partial u}{\partial r} - r'\frac{\partial u}{\partial z}\right) \tag{4.10}$$

The trajectory equation defines the position where the ion hits the detector. It means it can be used for finding of an optimal focus(ion detector).

In order to define the resolution of the spectrometer, one must let a number of ions fly with different initial conditions. (The resolution is defined as $\frac{t}{\Delta t}$). Let us introduce 100 ions. For each of 100 ions there is a certain flight time. One can assign values of t, the mean flight time and Δt is the deviation from mean t. In this section the *'standard deviation'* is applied to define the time and the mass resolutions.

One hundred ions will hit the ion detector at different positions, some of those will fly away. Changing the distribution of the potential one can find an appropriate distribution for which the focusing capability is good. The time dependent equations becomes

$$\frac{d^2r}{dt^2} = \frac{q}{m}\frac{\partial u}{\partial r} \tag{4.11}$$

$$\frac{d^2z}{dt^2} = \frac{q}{m}\frac{\partial u}{\partial z} \tag{4.12}$$

The time resolution of the spectrometer is defined (using above equations) in a way as follows. The flight time of 100 ions is approximated by Gauss distribution and a parameter σ characterizes the time resolution. By an adjustment of the distribution of potentials, one can find the distribution for which the time resolution is best.

Using the trajectory equation and time dependent equations, one can find the configuration of an electric field for which the spatial focusing and the time resolution are sufficient.The further one dimensional equation of motion 4.12 ($\frac{dr}{dt} = 0$) was used in order to find the optimal length of the reflectron.

4.1.2 The reflectron length estimation

In order to estimate the reflectron length one can use a one dimensional equation of motion for each region of the time-of-flight mass analyzer. The mass analyzer can be divided in four parts.

1. Acceleration region.
2. First drift region (field free region).
3. Reflectron.
4. Second drift region (field free region).

For each region the time-of-flight is defined in accordance with the following equations:

$$t_1 = \frac{\sqrt{2S_1}}{a_1} = md_1\frac{\sqrt{2S_1}}{qU_1} \tag{4.13}$$

$$t_2 = S_2/v_2 \tag{4.14}$$

$$t_3 = 2\frac{\sqrt{\frac{2E_k}{m}}}{qU_2} \tag{4.15}$$

$$t_4 = S_4/v_4 \tag{4.16}$$

where x is the x coordinate, a is the acceleration and t_i is the time-of-flight.

The hypervelocity dust particle impact will produce the ions with a certain distribution of initial kinetic energy. Actually the ions have a continuous distribution of the velocity components v_x, v_y, v_z. E_{init} is believed to have a Bolzman distribution. 90% of this distribution should be in the region from 0 to 30 eV, and the angular distribution has to obey the cos^2 law [40]. One can consider a situation when the changes of E are small and the E_r radial component is equal to zero. The electric field value E in the reflectron depends on z in this case. The ions will be accelerated in the electric field and will be reflected (at a reflectron) to the detector.

It was the idea of Mamyrin [37] to use the reflectron for compensation of the difference in initial kinetic energies. The ions having a higher energy go deeper into the electric field and spend more time in the reflectron. Thus the total flight time is similar for the ions of the same mass.

One can consider two ions, generated with different initial kinetic energies, namely 0 and 30 eV. The ions are accelerated in the electric field and are reflected to the detector. Fig. 4.1 shows the trajectories of two ions. The ion with an initial kinetic energy of 30 eV goes deeper into the reflectron and spends more time in the reflectron than the ion with zero initial kinetic energy. Changing the distances I,II,III,IV one makes it so that the time-of-flight of these two ions will be

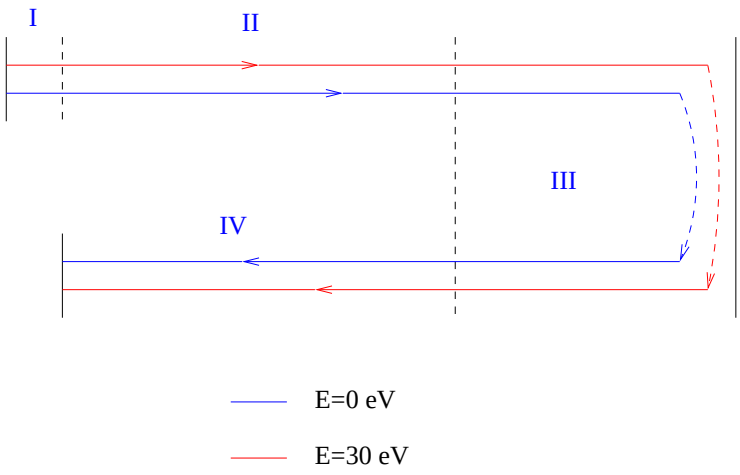

Figure 4.1: This picture explains the compensation for the difference in initial energies of two ions. The ions have a motion along the z axis only. For convenience, the return movement is transferred to the lower position. Two lines are the trajectories of the ions. The blue line corresponds to the ion with zero energy, the red line corresponds to the ion with an energy of 30 eV. Region I is the acceleration region. Regions II and IV are field free regions, where ions drift. Region III is the reflectron region.

equal. This idea was used to find the optimal length of the reflectron when using one thousand ions with given energy distribution. In these calculations, the lengths of regions II and IV were fixed to 0. The length of region I was 50mm.

Figure 4.2 shows that the best mass resolution one can achieve is 700 for the reflectron length of 400 mm.The mass resolution is defined as $\frac{m}{\Delta m} = \frac{t}{2\Delta t}$. This calculation was done for 100 ions with energies from 0 to 30eV. The ions have a direction of flight only along the z axis.

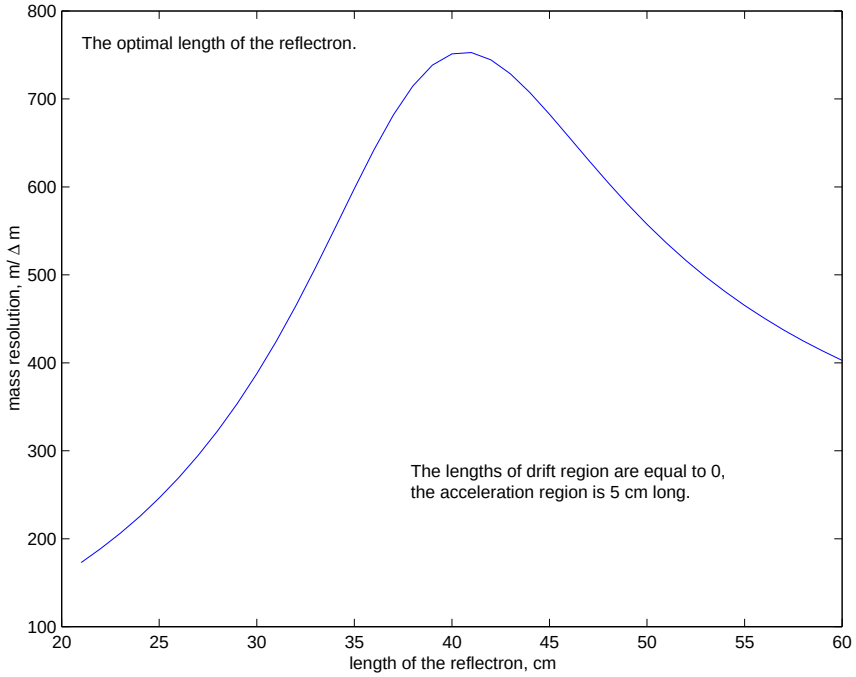

Figure 4.2: This figure shows a dependence of the mass resolution on the length of the reflectron. The mass resolution is maximal if the length of the reflectron is equal to 400mm.

The value of the calculated flight time was compared with that from the *SIMION* simulation. Even for this simplified case, the difference is small. However for the simplified case it is impossible to get a value for the transmission. The next step is to apply the trajectory equation as mentioned above. The potential distribution $u(0,z)$ along the z axis is in the form of $a\sqrt{z}+b$ (it was found from *SIMION* simulations). By slightly varying the constants a and b, one can find the potential distribution u(r,z) for the best transmission and the best time (mass) resolution.

A task for the future is to find the appropriate potential distribution. One can also try to use the solutions which are already derived. Several investigators studied appropriate potential distributions for the time-of-flight analyzers. Makarov A.A. [46] proposed to use the potential distribution $u(r,z)$ as $u = a(r^2 - 2z^2)$, where a is a coefficient to be determined.

For this one dimensional case, the strong statement was considered. The electric field is a constant inside the reflectron. If not the case, some difficulties exist.

4.1.3 A numerical method

While the analytical methods can be used only for a few cases, the numerical solutions exist in most cases. Computer implementation allows us also to visualize the field distribution, geometry, trajectories of the ions and many other parameters and options. Amongst different programs that utilize numerical solutions, the *SIMION* 7.0 software is used. The *SIMION*7.0 is software to solve the electrostatic and electromagnetic problems, and was developed at the Idaho National Engineering and Environment Laboratory [42]. It uses two kinds of files. The first file describes

the potential arrays which define the geometry and the potentials of the electrodes. The second file describes the initial conditions of the ions (energy, direction of flight, positions where ions are generated.) One can control individual runs using the *SIMION* programming language. The potentials inside of the electric field are defined by the Laplace equation $\Delta E = 0$. The Laplace equation is solved by *Finite Difference Method* [42] In Cartesian coordinates x, y, z the second derivative for x is.

$$\frac{\partial^2 u}{\partial x^2} = \lim_{\Delta x \to 0} \left[\frac{\partial u}{\partial x_i}(x+\Delta x, y, z) - \frac{\partial u}{\partial x}(x, y, z) \right] \tag{4.17}$$

$$\lim_{\Delta x \to 0} \left(u(x+\Delta x, y, z) - 2u(x, y, z) + u(x-\Delta x, y, z) \right) / (\Delta x)^2 \tag{4.18}$$

Similarly for y and z. Substituting this into the Laplace equation with $\rho = 0$ and $\Delta x = \Delta y = \Delta z = \delta$, where δ is a finite quantity gives

$$u(x+\delta, y, z) + u(x, y+\delta, z) + u(x, y, z+\delta) + u(x-\delta, y, z) + u(x, y-\delta, z) + u(x, y, z-\delta) = 6u(x, y, z) \tag{4.19}$$

This means that an electrical potential u, at an arbitrary point a(x,y,z) is defined as a mean of 6 neighbor points [45]. The search for an optimal geometrical configuration of the spectrometer was done in two ways. The analytical solution is helpful to find a general assumption (approximate geometry) while the *SIMION* simulations deals with the more detailed geometry of the instrument.

4.2 Geometric configurations

The difficulty of finding the optimal configuration is solving a large number of parameters like electrode configuration, the distance between them, voltage ratios and aperture sizes, all this in a simple case. Analytical solutions for the electric field distribution are found only in the simplest cases (symmetrical geometry with particles flying close to axis of symmetry, see above). For most of the considered cases, trajectories of the ions are very close to symmetry axes, and this is solved using the so-called paraxial equation. For a realistic large area configuration this is not the case. The width of the spectrometer is comparable with its length. The ion trajectories can be very far from the symmetry axis of the spectrometer. Because of these problems solutions are sought by trial and error in an intuitive way. During this process, significant experience has been gained. We have constructed a cylindrically-symmetric model of the mass spectrometer, consisting of the target area with an acceleration grid and potential rings between target and acceleration grid, providing a smooth electric field even close to the edges, and a single- or two-stage reflectron, the central ion detector, and an appropriate number of potential rings (Fig.4.3). Ions of varying starting positions(at the target), emission angles and energies are flown through the spectrometer. The potential of the second grid (U_{R2}) of the reflectron is varied under program control in order to find the axial position of the ion detector with optimum spatial and time focusing. It consists of three elements: an impact detector, a single or two-stage (shown) reflectron, and an ion detector which are separated by distances d_{t1} and d_{t2}. The impact detector consists of the impact target at a potential of 5000 V and a grounded acceleration grid, 50 mm in front.

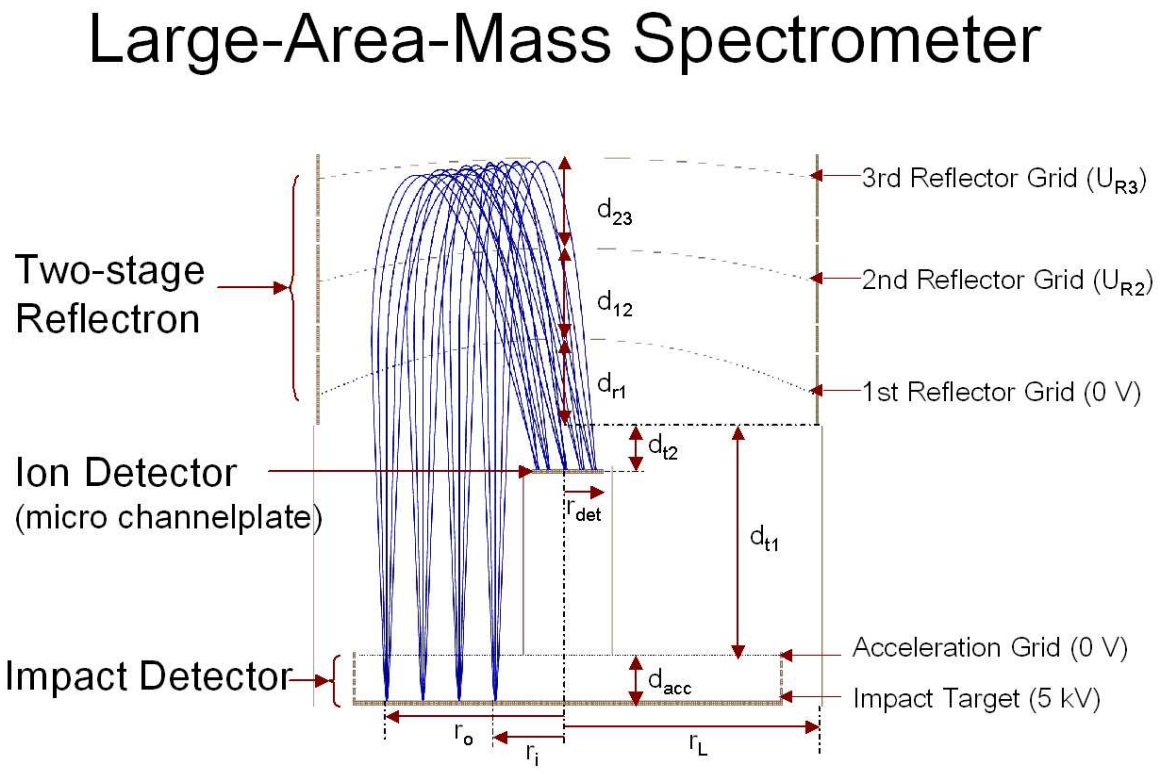

Figure 4.3: General assumption on the large area mass analyzer. The task is to define values of the parameters. The lines are the ion trajectories. All the ions form three group with the different starting position. They start at the impact target and are focused on the ion detector.

The reflectron is located at a distance d_{t1} in front of the target. It consists of two (single-stage) or three (two-stage) curved grids. The inner (first) grid is at ground potential and has an apex distance of d_{r1}. The apex of the second grid is at a distance of d_{12} from the first one. Its potential U_{R2} is varied. The apex of the third grid is at a distance of d_{23} from the second one. Its potential is fixed at U_{R3} = 5.1 kV. The reflectron grids were of parabolic shape and the distance between the grids was varied. The distance between the first and last grid (d_{12} + d_{23}) was varied between 250 and 500 mm, and the distances d_{t1} and d_{t2} were varied between 0 and 300 mm. Ions were launched from the target at several positions between distances r_i and r_o from the center at energies between 0 and 50 eV. Ion emission angles were varied between 0 and 90 degrees from the target normal, at various azimuth angles. The flight times, (tof_i) and the radial distance (rad_i) from the axis in the detector plane are determined for all ions *i*, from 1 to n, where *n* is the total number of ions tested, typically *n* is 100 to 1000 per impact position. The task was first to coarsely explore the geometric parameter space, and then to refine the best solutions and find the reflector grid voltage U_{R2} at which a high mass resolution and a small detector radius is obtained. We define here the mass resolution for each impact position by

$$\frac{M}{\Delta M} = mean(tof_i)/(2 \times (max(tof_i) - min(tof_i)) \tag{4.20}$$

(notice that this definition is different from the FWHM mass resolution used elsewhere) and the maximum radial distance (beam radius) in the plane of the ion detector by

$$r_{det} = max(rad_i) \tag{4.21}$$

One of the first results is that ions with different perpendicular (to the sensor axis) energies will arrive at the ion detector at different radial positions, with zero perpendicular energy in the center. Since the ion beam radius at the detector was found to be much bigger than the radius of the ion detector (micro channelplate), only the center of the ion beam will be used for the mass spectrum. A second result is that the maximum radial distance r_{det} is generally bigger for bigger d_{t1} and d_{t2}. Therefore, small values for d_{t1} and d_{t2} are preferred. Figure 4.4 shows the dependence of the beam radius r_{det} on the mass resolution $\frac{M}{\Delta M}$ for a single stage reflectron. Best values of $\frac{M}{\Delta M}$ 170 are found for r_{det}=110 mm.

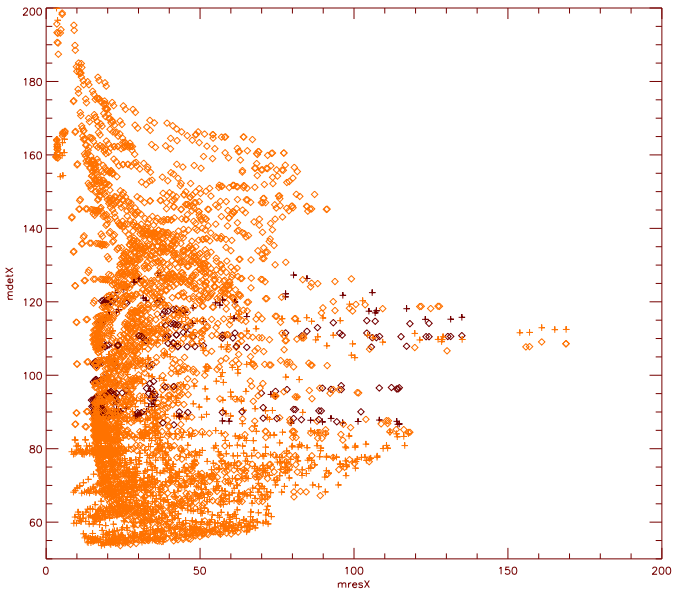

Figure 4.4: A Dependence of the beam radius r_{det} on the mass resolution $\frac{M}{\Delta M}$ for a single stage reflectron. Best values of $\frac{M}{\Delta M}$ 170 are found for r_{det} 110 mm. E.Gr¨un

This configuration of electrodes providing the best mass resolution $m/\Delta m = 170$ was chosen for further investigations, and is discussed in the next section.

4.3 Large Area Mass Analyzer, (LAMA)

The Large Area Mass Analyzer has a cylindrical symmetry (Figure 4.5).The detector is located in the center. The design has a system of concentric rings, a planar plate and two parabolic grids . The target consists of a short cup and four concentric rings with potentials uniformly distributed from 0 to 5kV. The acceleration region has a length of 5 cm. The plane target, the grounded grid and four concentric rings form the electrostatic acceleration field. The reflectron has a length of 400 mm and consist of two grids and nine concentric rings with non-uniform potential distributions. The reflectron grids have parabolic shapes. The potential is adjusted to have the proper value of electric field E_y. The area between the reflectron and the acceleration region is field free. Its length is adjusted to achieve best focusing and best mass resolution.

The best configuration for a single stage LAMA (E. Grün, personal communication) was obtained with the parameters given in Table 4.1. The rotationally symmetric parabolic grids are defined by the parabola:

$$y = \frac{x^2}{4 \cdot fo} \tag{4.22}$$

with focus offset fo. The total height of LAMA is 756 mm ($d_{acc} + d_{t1} + d_{r1} + d_{12}$) and the total width is 648 mm ($2 \cdot r_L$). There are several potential rings between the target, acceleration and reflectron grids in order to provide smooth electric field in the region of the ion trajectories: there

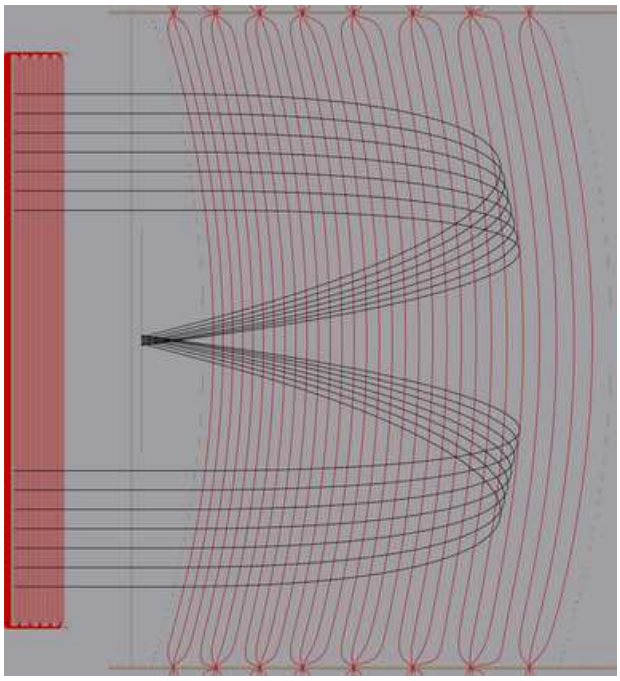

Figure 4.5: LAMA configuration with potential lines and some axial ion trajectories.

d_{acc}	d_{r1}	d_{12}	fo_1	fo_2	d_{t1}
50mm	231mm	400mm	500mm	500mm	75mm
d_{t2}	r_i	r_o	r_L	$\frac{M}{\Delta M}$	R_{det}
0mm	128mm	240mm	324mm	168.8	108.8mm

Table 4.1: Geometric parameters of LAMA configuration, version I.

are 4 equidistant potential rings between the target (5000 V potential) and the acceleration grid (0 V). There are 9 potential rings between first and second reflectron grid. In the reflectron ions reach a radial distance of 273 mm and approach the outer wall to 47 mm. This distance can be cut in half (consequently reducing the total diameter of the sensor) if the number of potential rings is increased by a factor 2. Also the total length can be reduced by up to 50 mm by bringing the outer reflectron grid closer to the inner one. Since only the field between the two reflectron grids matters there can be support structure for the grids outside this field region.

Characteristics of the solution are shown in Figure 4.6 on the left. The beam radius at the position of the ion detector is shown in blue. Since the ion beam radius is bigger than a realistic ion detector (micro channelplate) the mass resolution (red) is given only for ions that reach an ion detector of 25 mm radius. On the right, the ion beam radius at the ion detector is shown as a function of ion energy (or better as function of the speed component in the plane of the target). All ions with energies 2 eV will reach an ion detector of 25 mm radius, but also ions with higher energies will reach the detector if their in target plane speed component does not correspond to

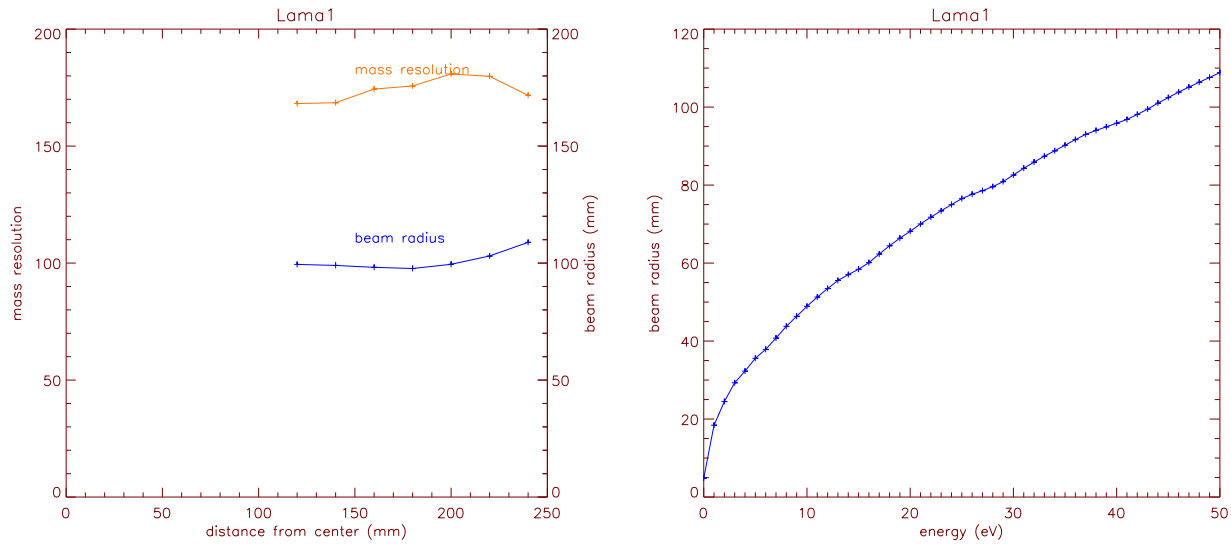

Figure 4.6: Mass resolution corresponding to ions that reach the ion detector of 25 mm radius and beam radius at the position of the ion detector as a function of the ion start position. *E.Grün*

energies exceeding 2 eV.

A three dimensional view of the analyzer is shown on figure 4.7. Through two cuts one can see the target, narrow field free region and grids of reflectron.

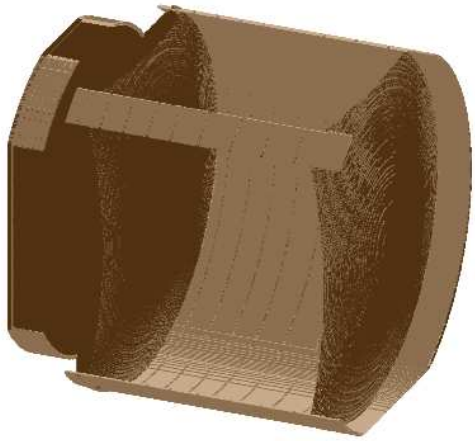

Figure 4.7: Large Area Mass Analyzer. This is 3-dimensional view of LAMA geometry configuration. Three cuts of the surface were done. One can see two reflectron grids and the target on the left side.

In Figure 4.8 a mass line (M = 100 amu) is shown for various ion start positions. The mass lines corresponds to ions that reach the ion detector of 25 mm radius. The mass scale shown on the top corresponds to the impact position 120 mm from center and 0 eV energy.

The considered large area mass analyzer can determine a chemical composition of dust particle. A trajectory sensor can determine mass, velocity and particle's trajectory. Therefore the

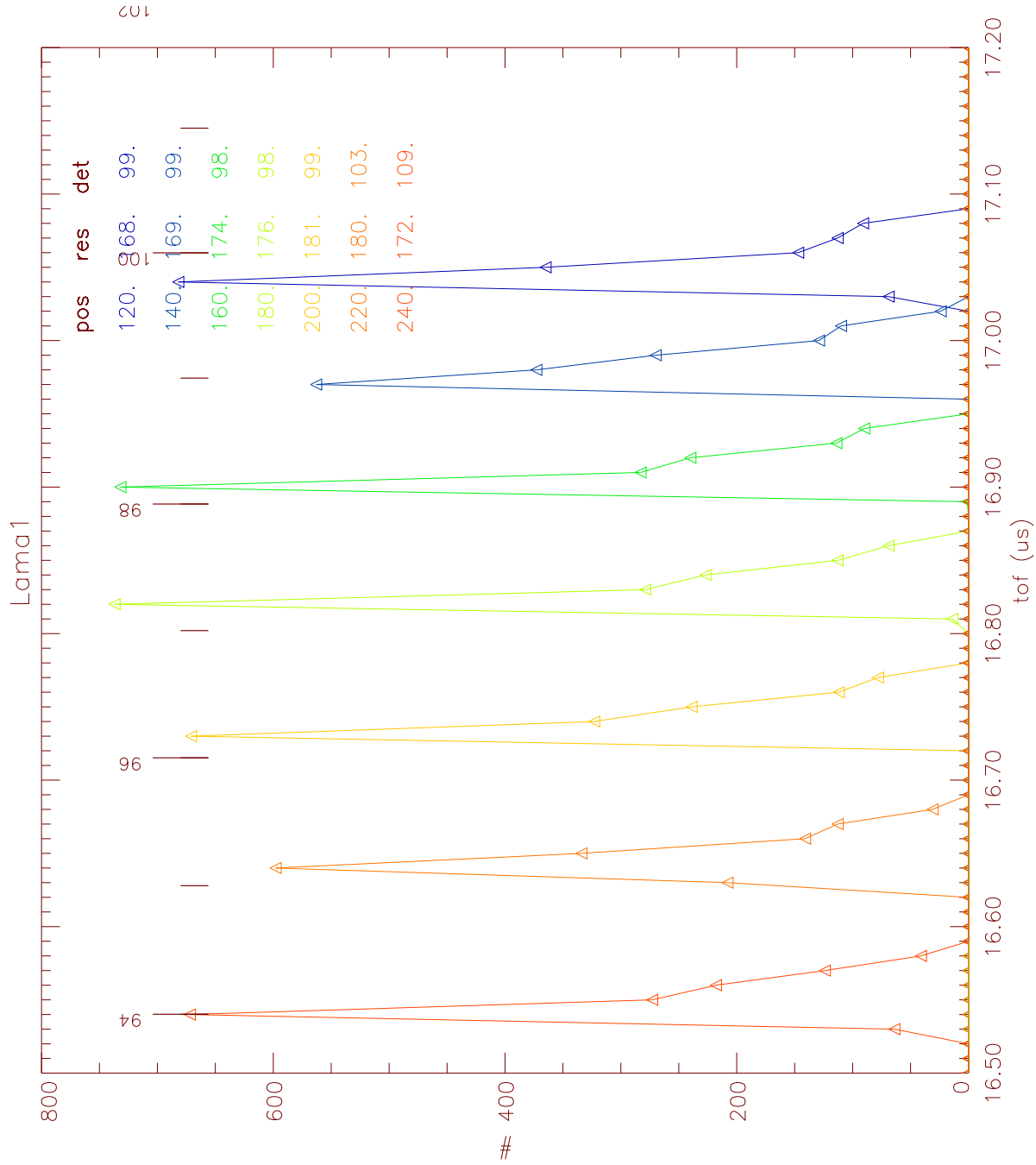

Figure 4.8: A mass line (M = 100 amu) is shown for the various ion start positions. The mass lines correspond to ions that reach the ion detector of 25 mm radius, *E.Grün*

mass analyzer has to be combined with the Trajectory Sensor that is discussed in the proceeding section.

4.4 Combination of the LAMA with a trajectory sensor

The new cosmic dust sensor is a combination of the trajectory sensor[1] and the chemical mass analyzer. For this reason the trajectory sensor has to be incorporated into the mass analyzer. One option is to put the trajectory sensor on the top of the mass analyzer. Another possibility is to put it between impact target and the reflectron. In the second case there is no need to introduce additional grid in order to shield a high voltage of the reflectron grid which is 5kV. Indeed the trajectory sensor in this case is placed between two grounded grids. For this case the geometry of LAMA should be changed in order to have enough space for the incorporated trajectory sensor.

The length of the trajectory sensor can be reduced to 170mm. Even if the LAMA is elongated, it has to show the mass resolution above 100. That is possible if the focal lengths of the parabolic grids will be changed as well.

Three configurations were found to be convenient. One of those was chosen, investigated and improved. This configuration is shown on figure 4.9. It differs from the first version by the use of a larger field free region, and a different curvature of the first reflectron grid. The parameters of new configuration are presented in a table 4.2.

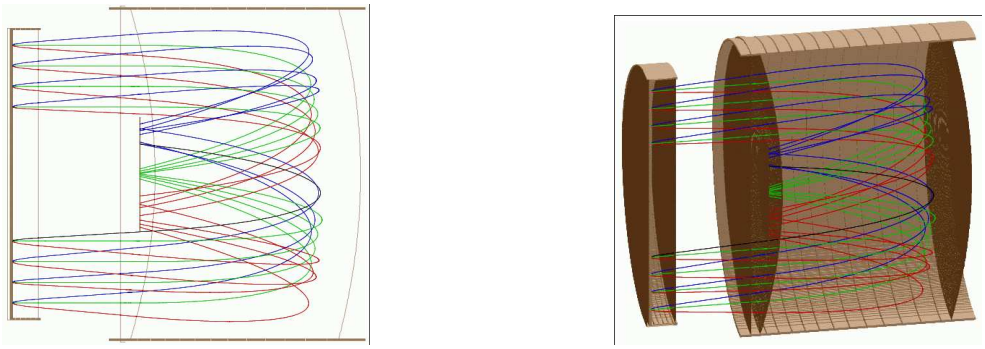

Figure 4.9: Large Area Mass Analyzer, version II. The fi eld free region is increased in order to insert the trajectory sensor.

The designed configuration has the mass resolution above for different impact positions. The resolution is better on outer region of the sensitive area and it is smaller near the center. Because the field free distance is increased, the beam diameter of incoming ions on the detector plane is increased as well, and is now about 12cm. This size of the ion detector allows the collection of all the incoming ions emitted at every impact position.

[1] the trajectory sensor defi nes the mass, velocity and trajectory of cosmic dust particle

parameter	LAMA I	LAMA II
target radius, mm	280	280
height of acceleration region, mm	50	50
height of field free region, mm	65	170
focus of first parabolic grid, mm	500	540
focus of second parabolic grid, mm	500	600
reflectron height on symmetry axis, mm	400	400
radius of reflectron, mm	320	320

Table 4.2: The LAMA I and the LAMA II. The parameters of geometric configuration.

4.5 Conclusion

During long investigation and modeling of different configurations of time-of-flight mass analyzers, one configuration was found. The investigation was done using Simion simulating software comparing geometries with different geometric parameters. The 1-dimensional estimation of the reflectron length was done. The result of the estimation is in accordance with that was got from the Simion simulations.

This configuration has a mass resolution above 100 for ion mass of one hundred. This mass resolution is valid for all impact positions at the impact target. The sensitive area is above of $0.1m^2$. The acceleration distance was set to 50mm. According to preliminary specifications the acceleration distance was set to 50mm. The reflectron voltage was chosen at 5kV providing better focusing.

In order to combine the Large Area Mass Analyzer and the trajectory sensor several geometric parameters were changed. These changes include the different focal distance of the parabolic grids and the different field free distance. The mass resolution is still above 100. In the next chapter some improvements of LAMA II will be described, and the resulting mass resolution of LAMA II will be compared to the mass resolution of LAMA I.

Chapter 5

Characteristics of LAMA

In the previous chapter, the basic LAMA design was described. Here some improvements will be considered, as well as the preparation of LAMA manufacturing. The simulation precision, possible grid deviation of ideal form and grid simulations of different thickness and different pitch size will be considered too.

The detection area of LAMA is large. There is no commercially available MCP detector of such size. In order to avoid the means of a big ion detector, an ion-to-electron converter was designed which would convert incoming ions to electrons and focus them to the MCP defector of usual size.

In order to smooth out the electric field inside the reflectron and improve mass resolution, the number of potential rings in the reflectron was increased.

5.1 Potential rings

The Large Area Mass Analyzer has a reflectron with a length of 400mm. On the reflectron boundaries there are nine concentric rings whose length is 41-42mm. Equipotential lines near these rings are irregular ones, and therefore one can assume large changes of electric field there. Hence the ion trajectories are distorted near the rings that causes a decrease of the mass resolution. In order to fix this problem the number of concentric rings has to be increased and placed at the proper location. Figure 5.1 shows a voltage dependence near the rings. Ideally the equipotential lines near the potential rings has to be smooth having a shape close to the parabolic one.

Three methods were applied in order to define the location of new rings, and voltages on them. All methods use the defined values of the field far from the reflectron wall.

In first method the voltage functions $V = f(z)$ are measured for different values of radius r.These functions can be presented as $V = az^2 + bz + c$, with coefficients a,b and c. Then the $V = F(r,z) = F(a(r),b(r),c(r),z)$ can be found approximating the dependences $a(r)$, $b(r)$, $c(r)$

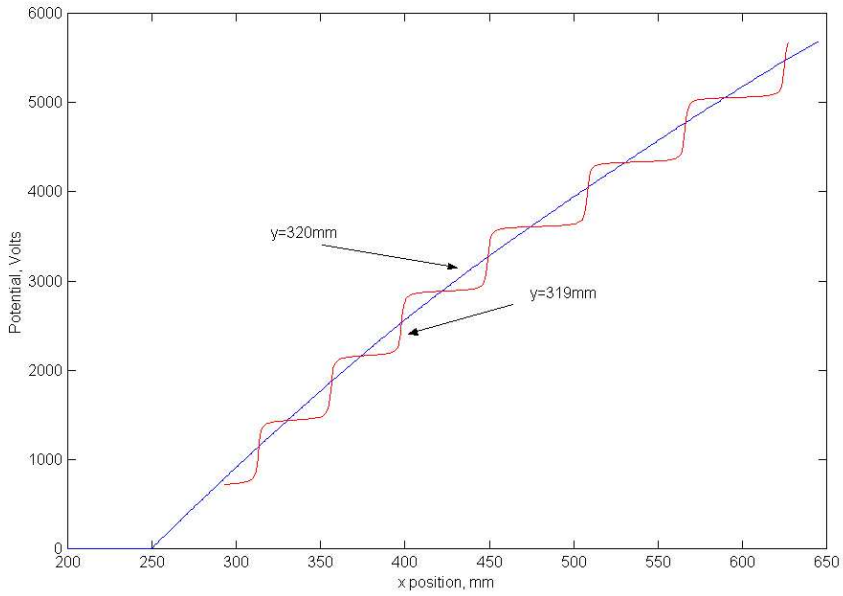

Figure 5.1: Voltage versus height of the reflectron, the radial position is fixed. This figure show the voltage dependence inside the reflectron for LAMA II version. The notes are made in Simion system of coordinate. The x is the z and the y is the r in cylindric system of coordinates

from the equations below.

$$\begin{array}{ll} 1 & V_1 = a_1 z^2 + b_1 z + c_1 \\ 2 & V_2 = a_2 z^2 + b_2 z + c_2 \\ 3 & V_3 = a_3 z^2 + b_3 z + c_3 \\ \ldots & \ldots \\ n & V_n = a_n z^2 + b_n z + c_n \end{array}$$

Here the r is a radial position, the z is z-coordinate in cylindric coordinate system. The new number of rings with assigned voltage has to be placed in accordance with the voltage function $V = F((r,z)$ found.

The second option is to use a series expansion for a voltage function in a case of axial symmetry.

$$u(r,z) = \sum_{k=0}^{\infty} \frac{(-1)^k U^{(2k)}(z)}{(k!)^2} \left(\frac{r}{2}\right)^2 = U(z) - U'' r^2/4 - U^{IV}(z) r^4/64 \pm \ldots \qquad (5.1)$$

The function U(z) is a voltage dependence along the symmetry axis of LAMA.

The third option is an increasing radial size of the reflectron keeping the field (equipotential lines) unchanged and place concentric rings outside their real location. This allows us to measure the voltage at the location where the rings were placed before. In this case, the electric field is not disturbed, as the rings are far away. Then, in accordance to the voltage dependence, new concentric rings can be built. On figure 5.2 one can compare the mass resolution of

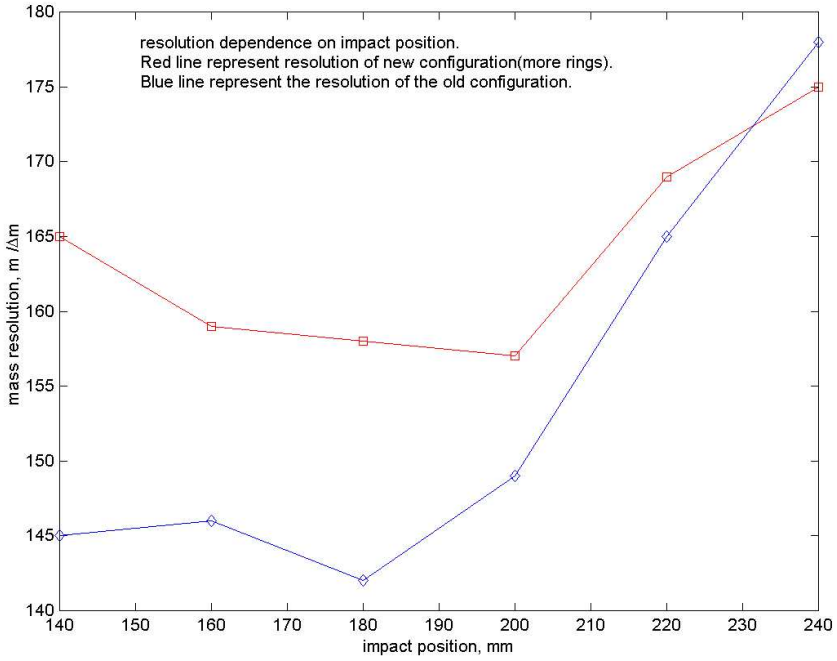

Figure 5.2: Mass resolution dependences for two LAMA configurations. One configuration has 9 concentric rings, another one has 13 concentric rings. The red line is almost all time above the blue one. The mass resolution

LAMA2(9 rings) and LAMA2(13rings). Here The LAMA2 is a second version of LAMA with the Trajectory sensor incorporated, see chapter 4.

In next section the simulation precision is described.

5.2 Precision of simulations

This section describes why the mass resolution depends on the simulation precision.

The Simion software defines values of field at certain points in 3D space. When calculating trajectories of flying particles, the software interpolates $\overrightarrow{E}$ the field between the points linearly. If the points number increases, the simulation precession increases too.

In practice, the simulation precision correlates to a manufacturing precision which consequently acts upon the focusing and the mass resolution. In the existing designs the simulation precision is 1mm. It means all electrodes are described by integer numbers. All float values are rounded to integer ones. For example there is no difference between 1mm and 1.4mm .

The $\overrightarrow{E}$ value is calculated at all points of so-called instance(a space where the instrument is considered) with 1mm distance between the calculated points. When the particle flies between the points, the $\overrightarrow{E}$ value calculated by an interpolation.

It should be taken into account that the number of points is limited. The higher the precision,

the smaller the amount of points considered.

For dimensions of about $650x710mm^2$ for the mass analyzer, the highest precision is 0.1mm. The considered number of points increases by 1000 times more as well as time necessary to calculate the electric field. The trajectory calculations become more precise, and it results in an increase of mass resolution from 180 to 220 for the one impact position with radial distance of 170mm. The transmission is 100 percents the same.

From the simulation with different precision, one can conclude that the manufacturing precision significantly influences the focusing abilities. In order to achieve a high resolution, the accuracy of calculations and manufacturing should also be high.

Another factor which affects the mass resolution and transmission is the grid dimensions.

5.3 Grid simulations

As well as for the discussed simulation precision one can assume other factors which might depose to focusing features. One of these factors is the dimensions of the grids. In simulations, the grids have no structure. It means all incoming particles pass through them and the field can not penetrate through the grid. There are two options when building non-ideal grids within the Simion environment.

One option is to rarefy the amount of points in a grid description. This approach allows the electric field $\overrightarrow{E}$ to penetrate through the grids. However the grids are not a barrier for the all of ions. In the case of rarefied points, one can find the optimal pitch of the wire mesh.

The result of this simulation is shown in a table 5.1. As one can see the optimal wire pitch is

pitch size, mm	mass resolution $m/\Delta m$
1	172.1
2	179.8
3	185.3
4	179.9
5	176.1

Table 5.1: The pitch size vs. mass resolution. For the axial symmetry the pitch size is represented by a distance between two concentric rings. These results are for the acceleration grid. This result can be explained The impact position is 240mm (radial position). The projectiles have a mass of 100 a.m.u.

3mm. The manufacturer proposed the hexagonal grid cell with a size of 0.7mm. In this case the wire thickness was also changed.

Another option is to build a grid as solid electrodes(cylinders). The LAMA should be separated into three parts, as the number of points becomes very high. For one part of LAMA, the simulation precision has to be increased by 10 times for example. Others instances have a precision of 1mm. The wires are build as curved rods with a square cross-section. As the program runs, it becomes very slow and only half of the wire mesh is used. The Simion's snapshot is shown on figure 5.3

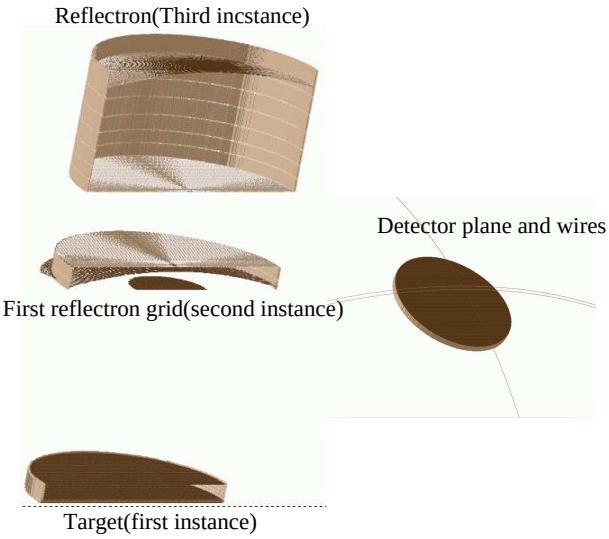

Figure 5.3: 3D LAMA configuration. The Analyzer is separated on 3 instances. The second instance includes 3D wire mesh. The wires are rods of parabolic shape. A detector and some of its wires are shown on the right part of the figure.

Choice between the wire size and the pitch is a trade off between transmission and mass resolution. The higher the pitch size (for a fixed wire cross-section) the higher transmission. However, the electric field can penetrate deeper through the grid mesh and distort the ion trajectories.

In practice it is also necessary to estimate the possible deviation of the grid shape from the ideal, mathematically described. This was done by inserting electrodes near the testing surface. The figure 5.4 presents the result of the simulation. The additional electrodes were of different sizes and located at different distances on the tested grid.

The next section is devoted to the ion-to-electron converter for the Large Area Mass Analyzer.

5.4 The ion-to-electron converter

The Large Area Mass Analyzer(LAMA) has a large sensitive area. The radius of the target is about 300mm, and an impact of a dust particle might occur at any target position. During the impact, a dust particle breaks-up into fragments and ions that are accelerated at 50mm distance between the target and the grid. After the transit trough the reflectron they are collected at the ion detector. In order to collect all of the ions, emitted at any position on the impact target and at any possible direction, we need a large area detector. In the design of The LAMA the detector is designated by a thin circle of 100mm radius.

The detector should be compact and light. It was assumed to apply a microchannel plate(MCP) detector. The MCP detector of such size is fragile and the output signal depends on the position of detection. Thus a special design of the MCP detector is required.

An alternative way is to build an auxiliary focusing system. The idea behind such a system

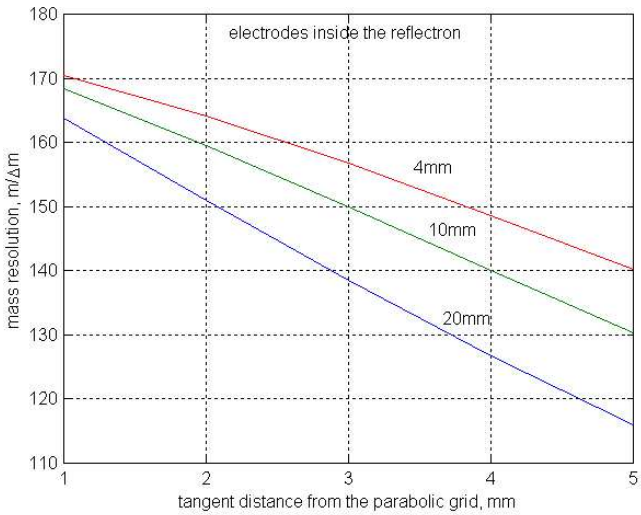

Figure 5.4: In order to investigate the possible deviation of grids of ideal shape one can insert the electrodes of different sizes near the parbolic grids. The electrode was placed near the second parabolic grid in the middle of the radial size of this grid. The mass resolution was checked for different distances from the electrode to the parabolic grid. The electrode sizes were 4mm, 10mm and 20mm.

is to detect the ions, and convert them to electrons that are focused to the MCP detector of usual size. The converter should have a steady mechanical structure, high efficiency, be compact, light and easy to operate. In early cosmic dust instruments the MM1 multiplier [47] was used as an ion detector, which proved its long life span. This multiplier consists of 20 perforated dynodes. The material of the dynodes is a CuBe alloy. A voltage of 2kV is uniformly distributed through the dynodes.

The incoming ions are converted to electrons on either first dynode or second one. The released electrons are accelerated in an inter-dynode space to an energy of about 100eV, hit next dynode and release other electrons with a conversion factor of 2. Eventually the multiplied avalanche is collected to an anode. The average multiplication is 2^{20}.

The focusing system consists of an electron converter, focusing electrodes and a microchannel plate detector. Two dynode stages are sufficient in order to convert ions to electrons. Indeed, two dynodes form the repetitive structure of the MM1 multiplier. Incoming particles can hit the first dynode, or fly through the holes to the second dynode. Released electrons are focused to pass through these holes.

In order to help electrons go through the dynodes they have a certain shape. A Priori this shape is unknown and it should be discovered.

5.4.1 Optimal geometry of the dynodes

In order to find the optimal geometry of the dynodes one has to consider some requirements.

One can characterize the converter by a transition time and a transmission. Since the tran-

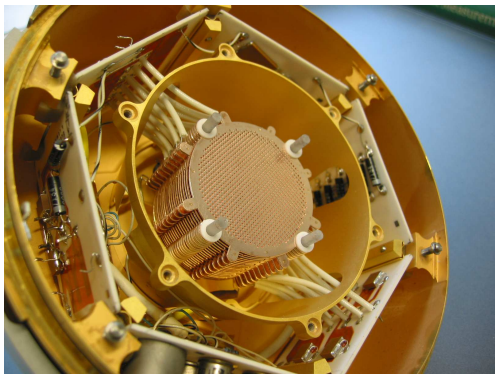

Figure 5.5: Spare ion detector unit of the Cassini cosmic dust sensor with the MM1 multiplier in the center. The multiplier consists of 20 and can be operated up to 4kV

sition time is defined by a transition time of incoming ions from one dynode to another one, it is possible to characterize the structure in terms of the transmission (incoming ions)/(released electrons reaching an anode) only. The transition time is always the same. Besides the optimal transmission one should take into account the reproducibility of possible structure. The designed dynode structure has to be reproducible using existing techniques.

Investigations of possible dynode structure were carried out in a close cooperation with Karlsruhe Research Center(Institute for Microstructures, IMT). They proposed to investigate techniques for the dynode manufacturing.

The MM1 dynode profile was measured in a laboratory of IMT and the profile was fitted using several functions. One good approach was to fit part of a sphere, see in fig.5.6. Such a consideration allows us to fit it to the top part of the dynode surface. Through both close viewing and measurements, it was noted that the surface of the MM1 dynode is not uniform. The average deviation of one tip from another one is about 10-30μ. The same accuracy was found for most repetitive cells of the MM1 dynode.

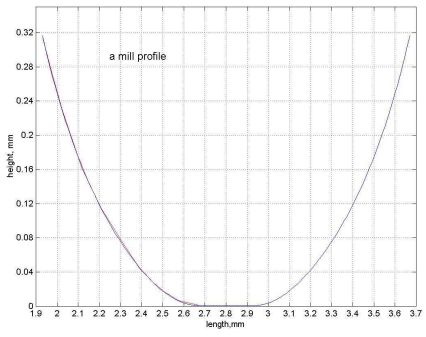

Figure 5.6: The fit function of the dynode profile formed by two parts of circle and linear function in a gap between the circles

geometry, type of tips	transition time	transmission, percents
cylinder	10ns	14-15
planar	10ns	10-12
rotational sphere	10ns	30-34
spheres cut	10 ns	40-45
paraboloid cut	10 ns	40-45

Table 5.2: Comparison of transition time and transmission for different types of tips

It is not clear whether the MM1 multiplier has the best configuration. Several models were thus built using the Simion7.0 simulation software. The computer model assumes analytically given surfaces, and voltage distribution over surfaces.The controlling programs were written to describe the behavior of particles moving through multipliers. For simplification it was assumed that one incoming ion releases one electron when hitting the dynode, and one accelerated electron releases just one secondary electron. The released electrons were assumed to be ejected at a normal direction in respect to the impact position. An ejection energy is randomly distributed over the 1-2eV region [48].

The geometries that have been investigated are shown on figure 5.7 and in table 5.2 . The most simple shape of the dynode is a plane. However, the value of transmission(incoming ions)/(released electrons reaching an anode) is only about 12 percent.

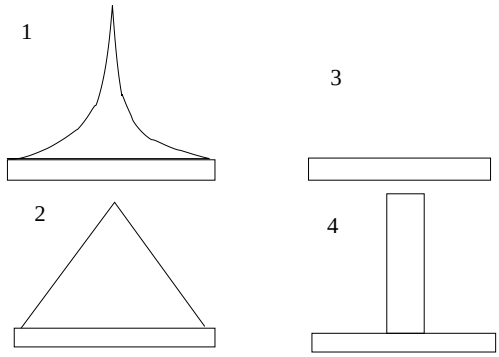

Figure 5.7: Different types of tips. For the first tip, one elementary cell is made by a rotated sphere. For the second one, the dynodes are planes with holes. The next tip has a conical surface. The forth tip has a cylindrical shape.

The best transmission has the geometry formed by a cut of four spheres. Such the formation can be made in a material using four milling tools of spherical shape, or by etching with spherical propagation.In fact, the structure of the dynode is very similar to the dynodes of the MM1 multiplier. The three dimensional view of this structure and the simulation procedure are shown in figure 5.8.

In simulations, the ions are converted to electrons when they hit the dynode. The electron with an energy of 2eV are emitted from the dynode at the direction of normal vector to the point

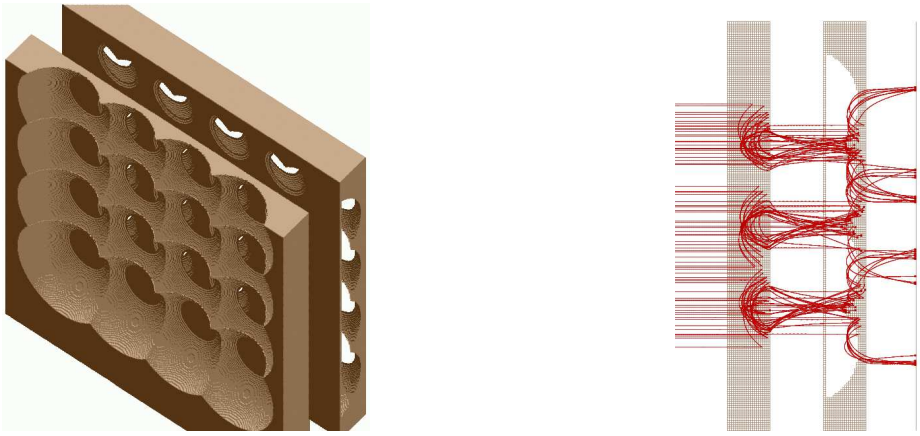

Figure 5.8: The designed structure of the ion-to-electron converter. The simulation procedure is shown on the right. The color lines are trajectories of the particles(ions and electrons).

of impact.Then the electrons are accelerated at an interstage space, they hit the next dynode and release other electrons. Such a process repeats until the electrons reach the anode. An optimal voltage for one stage was found to be $170V$. The transmission is of 0.44. The distance between the dynodes was optimized to $560\mu m$. By the next step, one must consider the manufacturing of its possible structure.

5.4.2 Manufacturing

In order to manufacture the dynodes, several processes of manufacturing were investigated(fig. 5.9). For simplicity the manufacturing of several types of dynodes were proposed. The best solution has the spherical shapes that could be produced either by machining, or etching. Since the ion detector has a large area, the number of holes an tips is very large (see tips on figure 5.7). One elementary cell has dimension of 1mm. $S_{detector} = \pi r^2 = 45000mm^2$. It means that the number of tips is about 4.5×10^4. In the case of machining, it takes about one day to manufacture a dynode of this area.

Some features of MM1 show that the multiplier was made by etching. The structure is irregular. One can see different diameters of holes, the holes sometimes have improper shapes and the height of one tip deviate from the height of another tip. The top of each tip is smoothed and rounded. Sometimes it looks pressed down. For the etching several masks, solutions and materials were investigated(Karlsruhe Research Center, IMT). Figure 5.10 shows the etching procedure and resulting irregular structures. Because of a lack of equipment, investigation of etching was not continued.

In fact, the dimensions of the dynode lie in the submicron range. In this range, machining can still be used. An advantage of machining that, it is a simple and flexible method. On figure 5.11 one can see the scanning electron microscope(SEM) picture of a promising dynode made by machining.

This structure seems to be quite close to that of MM1. The accuracy of manufacturing is of

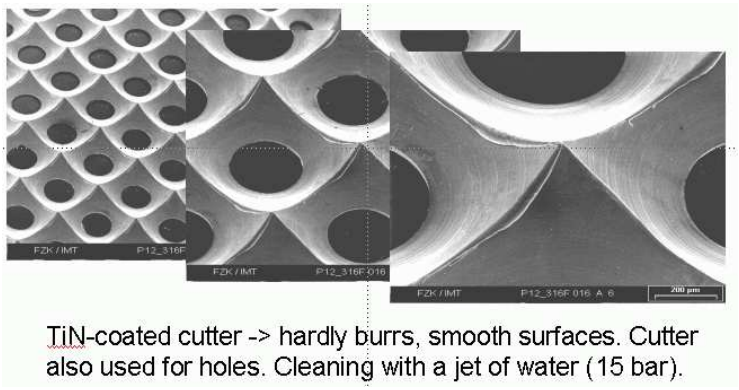

Figure 5.9: Machined dynode, different zoom.

the same order as for the simulations. The material of the dynode plate is a brass, other materials can be investigated too. It is also possible to get a desirable composition with a coating.

Some words should be said about the angle distribution of the ions. The auxiliary system was designed in order to collect all of the ions coming into the detector plane. Most of these ions are emitted at large angle (70-90 degree due to the normal vector of the impact target). If the direction of flight obeys a $cos(x)$ or $cos^2(x)$ law, then the ions don't contribute a lot. The number of ions corresponds to approximately 6 percent from total number of ions. So one would expect the charge produced by these ions to be on the noise level. This allows us to avoid detection of such ions, and thus reduce the detector area, and the area of the ion-to-electron converter.

5.5 Conclusion

The detector system of LAMA will consist of an ion-to-electron converter, the electron reflection system and the microchannel plate detector of usual size. The major part of the system is the ion-to-electron converter which will have structure similar to MM1 multiplier. An advantage of MM1 multiplier is its proven long life on board Cassini space mission. The time resolution of the converter is estimated by the transition time, and is about 10ns. The transmission (converted ions)/(all incoming ions) is about 0.44.

Several methods of manufacturing were considered, and the machining seemed to be optimal method.

Improvement of the LAMA characteristics was discussed in this chapter. Using the design of an ion-to-electron converter, one can collect all ions formed during the impact. An increase in the amount of potential rings increases the mass resolution. The grids simulation, and the estimation of manufacturing precision completes the design process, and allows us to manufacture the Large Area Mass Analyzer.

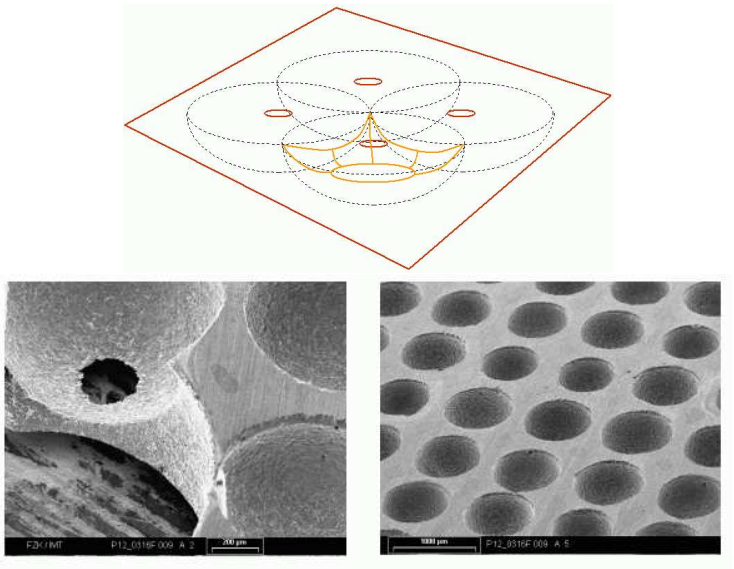

Figure 5.10: Etching process. The picture above shows how the etching process propagates through mask with holes. The pictures below shows the results of etching. The mask has a different diameters of the holes. Therefore the dynodes made have irregular structure

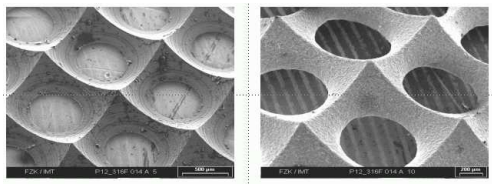

Figure 5.11: The most promising of the structures made by the machining

Chapter 6

Summary and Outlook

The present thesis reports on the development of a high-resolution, large impact area dust mass analyzer. The thesis has two aspects. Firstly, the set-up of a laboratory model of a high resolution mass spectrometer, like the ones flown on the space missions to comet Halley, and secondly, the development of a large area mass analyzer.

In order to learn more about the processes that accompanied the dust particle impact, the high resolution mass spectrometer was simulated and built. This spectrometer is a stand-alone instrument which incorporated into a vacuum chamber. Several pumps provide the vacuum (10^{-6} Pa) required for the microchannel plates (MCP) detector. It is possible to visualize the spatial distribution of the ions which were generated in a dust impact, using a phosphor screen just behind the MCP detector.

The measured spectra of high resolution mass analyzer were compared to the simulated spectra. Assumptions on the ions participating in simulations can also be made from the measurements. From the comparison one can see that the ions have narrower initial energy range than it was supposed in the simulations. The angular distribution is difficult to estimate, because of the instrument's aperture.

In general, the geometry of Large Area Mass Analyzer consists of the large number of the parameters which are very difficult to determine. So some assumptions have to be made. In order to find a suitable solution for the large area mass analyzer, several geometry configurations have been checked. All of those configurations include a reflectron for the compensation of the initial ion energy difference. All configurations have a very similar design. However the ion transmission of the spectrometer as well as the time and mass resolution strongly depend on how well the parameters of the reflectron are adjusted.

A mechanical and electrical configuration for a Large-Area Mass Analyzer was found when optimizing the geometry parameters. It has a ring-shaped target of $0.1m^2$ area. A reflectron focuses the ions that are generated at the target onto the central detector. The Large-Area Mass Analyzer has a mass resolution above 150, and the ion transmission is very high 100 % in the case of totally transparent grids. The detector has a radius of 120 mm. This large size is the price

for transmission of 100%. This size of the detector is required in order to collect all ions emitted into a hemisphere with initial energies up to 50 eV. The size of the detector can be reduced if the initial ion energies are lower or if the ions are emitted into a narrower beam. In case of a smaller ion detector, a correspondingly smaller fraction of the detected ions will reproduce the whole spectrum.

Another possibility to apply the MCP detector of usual size is to apply ion-to-electron converter in front of the MCP detector. The ions will be converted th the electrons which are focused onto the MCP detector. A design of the ion-to-electron converter is based on MM1 multiplier.

For ions of mass 100 a.m.u. the total flight time in about $17\mu s$. The flight time difference is a few ns for ions with different initial conditions. Thus the changing of parameters like the curvature of the grids, their positions or voltages will have an effect on the mass resolution. Therefore the sensitivity of the instrument performance on details of the instrument configuration were also checked.

Appendix A

Laboratory model of high resolution mass analyzer(pictures)

The high resolution mass analyzer is shown on two pictures. The first picture is a top view of the analyzer. One can see two arms and the reflectron volume. Red parts are the support for the instrument, and pumps. Each part(legs and reflectron) has a gauge in order to measure the vacuum inside the chamber.

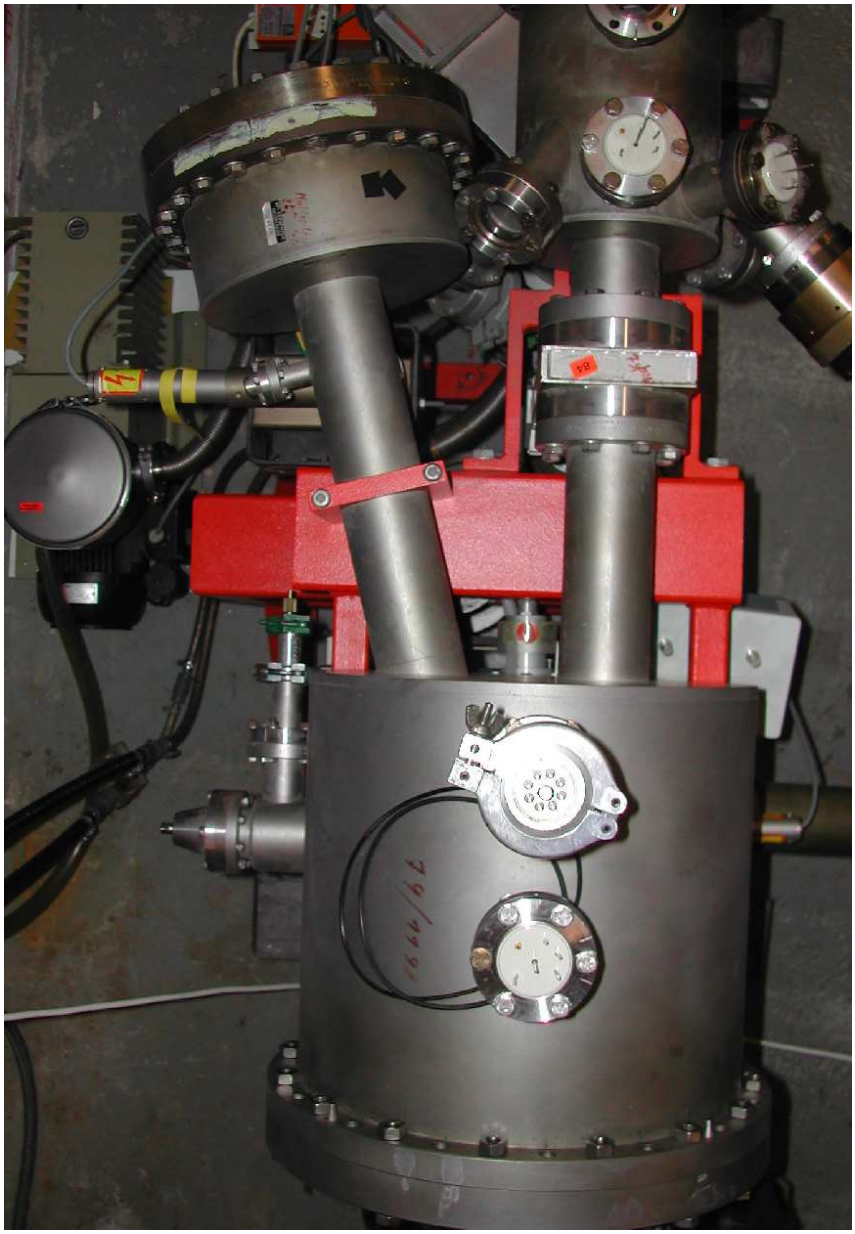

Figure A.1: Top view of the laboratory instrument. One can see vessels of the 2 legs and the reflectron.

The second picture shows the empty target volume and turbo pump just below it. The laser is situated on the left on the analyzer.

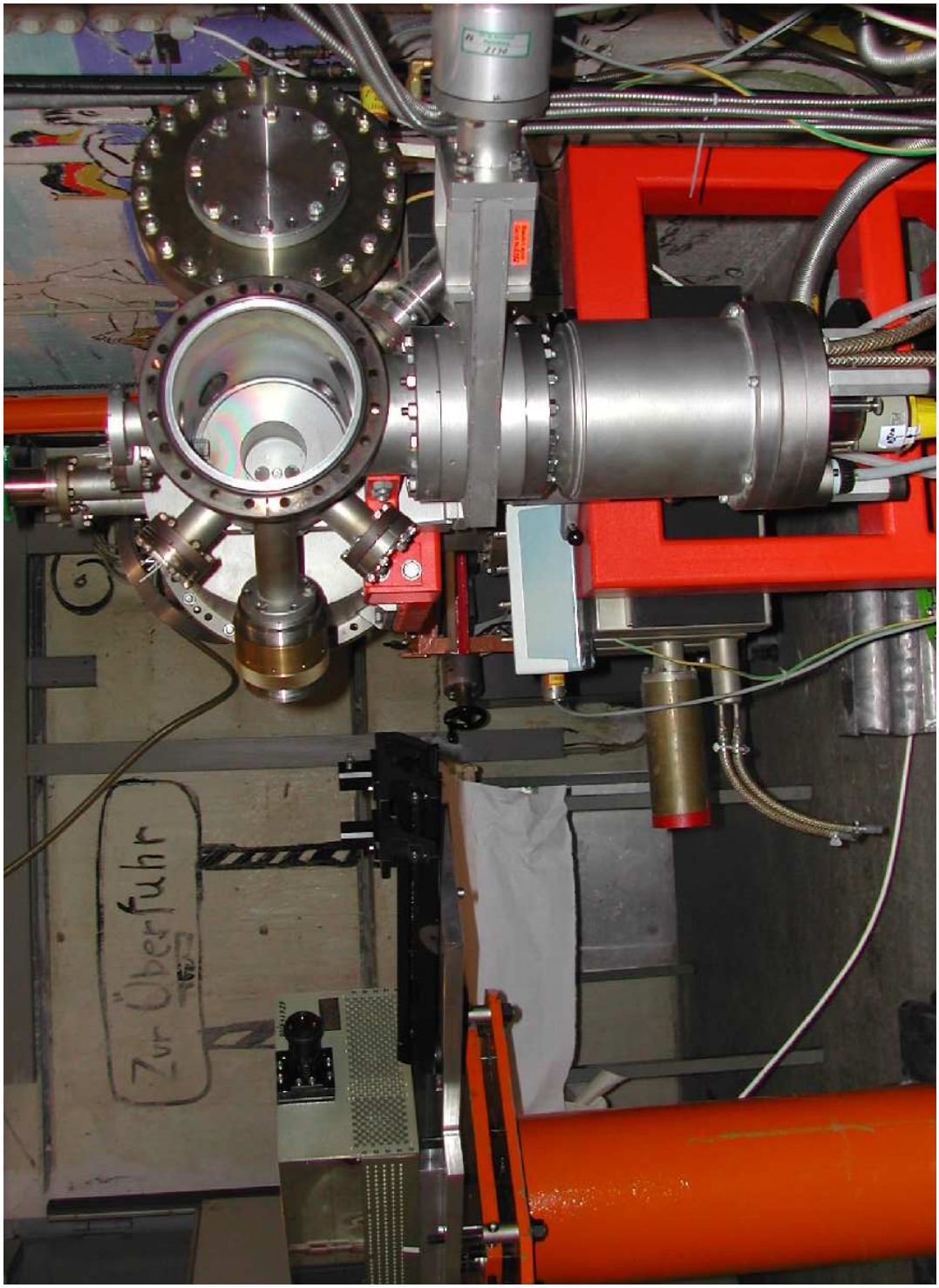

Figure A.2: Target volume. The laser set-up.

Appendix B

The geometry file of Large Area Mass Analyzer

The first step of our work is the creation of a geometry file. In the geometry file, the structure of electrodes (shapes, length, with, height,position, voltage) is described. Further, *SIMION* use this file for time-of-flight simulations. This chapter contains the file describing the geometry of Large Area Mass Analyzer and the picture of LAMA, version II .

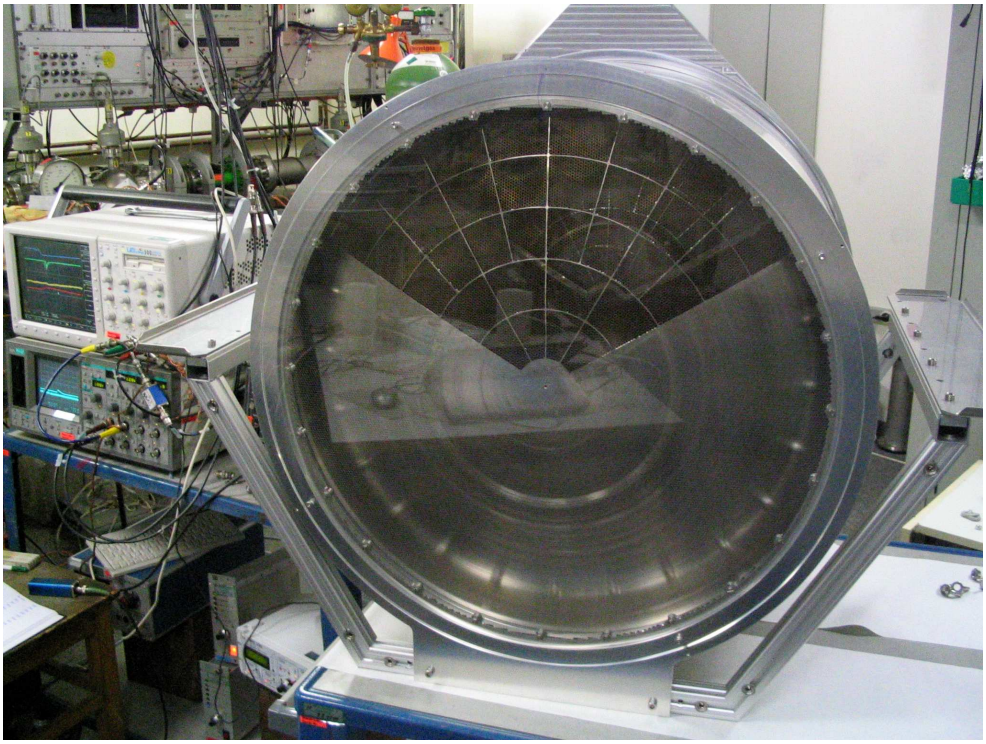

Figure B.1: The Large Area Mass Analyzer in the Heidelberg dust laboratory.

```
pa_define( 616, 330,1,cylindrical,y_mirror)       ;scale 1 mm/grid unit
locate(145)                                       ;
        {
        e(1)                                      ;1st reflectron grid
                {
                edge_fill{within{locate(,,,,,90){parabola(   0, -61, 500)}box( -10,

;parabola
                fill{within{box( -32, 320,  30, 323)}}
                }
        e(2)                                      ;3rd reflectron grid
                {
                edge_fill{within{locate(,,,,,90){parabola(   0,-461, 500)}}}
;parabola
                fill{within{box( 382, 320, 467, 323)}}
                }
        e(3)                                      ;9. pot ring r1-r2
                {
                fill{within{box(  32, 320,  72, 323)}}
                }
        e(4)                                      ;10. pot ring r1-r2
                {
                fill{within{box(  74, 320, 115, 323)}}
                }
 e(5)                                    ;11. pot ring r1-r2
                {
                fill{within{box( 117, 320, 157, 323)}}
                }
        e(6)                                      ;9. pot ring r1-r2
                {
                fill{within{box( 159, 320, 207, 323)}}
                }
        e(7)                                      ;12. pot ring r1-r2
                {
                fill{within{box( 209, 320, 265, 323)}}
                }
        e(8)                                      ;13. pot ring r1-r2
                {
                fill{within{box( 267, 320, 322, 323)}}
                }
        e(9)                                      ;14. pot ring r1-r2
                {
                fill{within{box( 324, 320, 380, 323)}}
```

```
                }
        n(0)
                {                                   ;remove false lines
                fill{within{box(   0, 324, 497, 330)}}
                }
         n(0)
                {                                   ;remove false lines
                fill{within{box(   0, 324, 497, 330)}}
                }
        e(0)
                {                                   ;detector + grounded box
                fill{within{box(   0,  -1,  -1, 110)}}
                }
        }
locate(20)                                          ;target level
        {
        e(10)                                       ;target
                {
                fill{within{box(-5,0,0,280)}}           ;target
                fill{within{box(-5,280,004,283)}}               ;target rim
                }
        e(11)                                       ;1. potential ring
                {
                fill{within{box(006,280,014,283)}}
                }
e(12)                                   ;2. potential ring
                {
                fill{within{box(016,280,024,283)}}
                }
        e(13)                                       ;3. potential ring
                {
                fill{within{box(026,280,034,283)}}
                }
        e(14)                                       ;4. potential ring
                {
                fill{within{box(036,280,044,283)}}
                }
        e(0)
                {                           ;acceleration grid and central box
                edge_fill{within{box(-10,-1,050,283)}}
                fill{within{box(046,280,054,283)}}
                }
        }
```

Appendix C

The geometry files of High Resolution Mass Analyzer.

This appendix contains the geometry files of the high resolution mass analyzer and the control programming file. The geometry configuration description consist of three files. The first file is a description of the first leg of the analyzer. The second file is a description of the second leg. The third file is a description of the reflectron. The control programming file contains instructions on how to optimize the electrode voltages.

C.1 First arm of the high resolution mass analyzer

```
pa_define(420,200,200,planar,non-mirrored)       ;scale 1 mm/grid unit
locate(10,100,100,1,-90,0,0){
         e(1){                                    ;focus ring1
                fill{within{cylinder(0,0,-100,40,40,10)}
                     notin{cylinder(0,0,-100,38,38,10)}}
                 }

         e(5000){                                   ;target
                fill{within{cylinder(0,0,-5,15,15,5)}}
             }
locate(0,0,-90,1){
         e(0){                                    ; grid
                edge_fill{within{cylinder(0,0,0,40,40,0)}}
             }
                }
locate(0,0,-120,1){
         e(0){                                    ; grid
                edge_fill{within{cylinder(0,0,0,40,40,0)}}
```

```
            }
               }

locate(0,0,-30,1){
         e(0){                                        ;acceleration grid
               edge_fill{within{cylinder(0,0,0,15,15,0)}}
            }
               }
 e(0){                                      ;acceleration grid
               edge_fill{within{cylinder(0,0,0,15,15,0)}}
            }
               }
locate(0,0,0,1){
   e(0){                                            ; guard tube
               fill{within{cylinder(0,0,0,23,23,40)}
                    notin{cylinder(0,0,0,22,22,40)}}
               fill{within{cylinder(0,0,1,23,23,1)}}}
              }
locate(0,20,-20,1,0,0,45){
   non_electrode(){                                                ; guard tube
               fill{within_inside_or_on{cylinder(0,0,0,2,2,10)}}}
              }

         ;e(0){                                        ;focusing target
         ;       fill{within{box(410,0,416,75)}}
         ;    }
         e(0){
               fill{within{cylinder(0,0,0,75,75,153)}       ;tube
                    within{cylinder(0,0,0,35,35,400)}
                     notin{cylinder(0,0,0,70,70,150,)}
                     notin{cylinder(0,0,0,30,30,400)}}
               ;edge_fill{within{cylinder(1,0,1,69)}}
           }
locate(0,35.3553,-45.3553,1,0,0,45){
   e(0){                                            ; laser_tube
               fill{within{cylinder(0,0,0,20,20,100)}
                    notin{cylinder(0,0,0,18,18,100)}}}
              }
locate(0,0,-310,1){
   e(2){                                            ; lens2
               fill{within{cylinder(0,0,0,25,25,90)}
                    notin{cylinder(0,0,0,23,23,90)}}}
              }
```

```
      }
```

C.2 Second arm of the high resolution mass analyzer

```
pa_define( 350,80,1,cylindrical,y_mirror)       ;scale 1 mm/grid unit
locate(0,0,0,1)
                        {

         e(-2000){                                        ;detector
                fill{within{box(10,0,11,40)}}
             }
         e(0){                                       ; 0 potential grid
               edge_fill{within{box(30,0,30,35)}}
             }

         e(0){ fill{within{box(30,0,330,40)}  ;tube
                    notin{box(30,0,330,35)}}
               fill{within{box(0,0,30,70)}
                    notin{box(0,0,30,67)}}
               fill{within{box(30,41,33,70)}}
               edge_fill{within{box(1,0,1,67)}}}

                        }
```

C.3 Reflectron

```
pa_define( 350,330,350,planar,e)       ;scale 1 mm/grid unit
locate(350,325,15,1,0,180,0){
locate(300,0,0,1,0,90,90){
   e(0){                                          ;tube
        fill{within{cylinder(160,160,25,160,160,300)}
                  notin{cylinder(160,160,25,157,157,297)}}}
}
locate(300,16,0,1,0,96,90){
e(0){                                        ;grid1 with 0 potential
        edge_fill{within{cylinder(160,160,21,130,130,0)}}}
```

```
e( 255){
    fill{within{cylinder(160,160, 15,126,126,6)}
                notin{cylinder(160,160, 15,122,122,6)}}}
e( 510){
    fill{within{cylinder(160,160,  3,126,126,6)}
                notin{cylinder(160,160,  3,122,122,6)}}}
e( 765){
    fill{within{cylinder(160,160, -9,126,126,6)}
                notin{cylinder(160,160, -9,122,122,6)}}}
e(1020){
    fill{within{cylinder(160,160,-21,126,126,6)}
                notin{cylinder(160,160,-21,122,122,6)}}}
e(1275){
    fill{within{cylinder(160,160,-33,126,126,6)}
                notin{cylinder(160,160,-33,122,122,6)}}}
e(1530){
    fill{within{cylinder(160,160,-45,126,126,6)}
                notin{cylinder(160,160,-45,122,122,6)}}}
e(1785){
    fill{within{cylinder(160,160,-57,126,126,6)}
                notin{cylinder(160,160,-57,122,122,6)}}}
e(2040){
    fill{within{cylinder(160,160,-69,126,126,6)}
                notin{cylinder(160,160,-69,122,122,6)}}}
e(2295){
    fill{within{cylinder(160,160,-81,126,126,6)}
                notin{cylinder(160,160,-81,122,122,6)}}}
e(2550){
    fill{within{cylinder(160,160,-93,126,126,6)}
                notin{cylinder(160,160,-93,122,122,6)}}}
e(2805){
    fill{within{cylinder(160,160,-105,126,126,6)}
                notin{cylinder(160,160,-105,122,122,6)}}}
e(3060){
    fill{within{cylinder(160,160,-117,126,126,6)}
                notin{cylinder(160,160,-117,122,122,6)}}}
e(3315){
    fill{within{cylinder(160,160,-129,126,126,6)}
                notin{cylinder(160,160,-129,122,122,6)}}}
e(3570){
    fill{within{cylinder(160,160,-141,126,126,6)}
                notin{cylinder(160,160,-141,122,122,6)}}}
e(3825){
```

```
    fill{within{cylinder(160,160,-153,126,126,6)}
                notin{cylinder(160,160,-153,122,122,6)}}}
e(4080){
    fill{within{cylinder(160,160,-165,126,126,6)}
                notin{cylinder(160,160,-165,122,122,6)}}}
e(4335){
    fill{within{cylinder(160,160,-177,126,126,6)}
                notin{cylinder(160,160,-177,122,122,6)}}}
e(4590){
    fill{within{cylinder(160,160,-189,126,126,6)}
                notin{cylinder(160,160,-189,122,122,6)}}}
e(4845){
    fill{within{cylinder(160,160,-201,126,126,6)}
                notin{cylinder(160,160,-201,122,122,6)}}}
   e(5100){                                        ;reflection grid
        edge_fill{within{cylinder(160,160,-223,140,140,0)}}}
   }
 locate(300,0,0,1,0,90,90){
   e(0){                                        ;plate with 0 potential
        fill{within{cylinder(160,160,-271,150,150,2)}}}
}
}
```

C.4 Control voltage file

In order to perform cycled search of the optimal parameters the *SIMION* has a special programming language. Below is the file that finds the optimal electrode voltage.

```
defa current_try 0
defa test_voltage1 0
defa terminate_after_run 0
defa t1 0
defa t2 0
defa ttemp 0
defa mean 0
defa sigma 0
defa sum_2 0
defa sum_21 0
defa mean_2 0
defa temp2 0
```

```
defa sum2 0
defa sum3 0
defa sum4 0
defa temp3 0
defa temp4 0
defa tempsigma 1
defa varf 1

Seg Other_Actions
 rcl Ion_Splat
 -1 x!=y exit

  rcl Ion_time_of_Flight
  rcl ttemp +
  sto ttemp
  ;mess   ; toft= #

  rcl Ion_time_of_flight
  rcl Ion_time_of_flight *
  sto sum_21
  rcl sum_2 +
  sto sum_2
  ;mess   ; suds= #
seg terminate
 rcl ion_number 6 x!=y exit

   rcl sigma
   ;mess ;    sigma1= #
   rcl ttemp 1000 /
   sto mean
   mess     ; mean= #

   rcl mean
   rcl mean *
   sto mean_2
   ;mess ; sum1= #
   rcl ttemp
   ;mess ;ttemp= #
   rcl mean *
   sto temp2
   rcl temp2 2 *
   sto temp3
   rcl temp3 1000 /
```

```
   sto sum2
   ;mess ; sum2= #
  rcl sum_2 1000 /
   sto sum3
   ;mess ; sum3= #

   rcl mean_2
   rcl sum2 -
   sto temp4
   ;mess ; temp4= #
   rcl temp4
   rcl sum3 +
   ;mess ; sum= #
   abs
   sqrt
   sto sigma

   mess     ; sigma= #

   rcl sigma                        ; change direction
   rcl tempsigma
   x<y goto flag1
goto flag0
   lbl flag1
   rcl varf
   1 sto varf
   lbl flag0
   rcl varf
   0 sto varf
;reset of variables
 rcl ttemp
 0 sto ttemp
 rcl mean
 0 sto mean
 rcl mean_2
 0 sto mean_2
 rcl temp2
 0 sto temp2
 rcl temp3
 0 sto temp3
 rcl temp4
 0 sto temp4
 rcl sum2
```

```
 0 sto sum2
 rcl sum3
 0 sto sum3
 rcl sigma
 0 sto sigma
 rcl sum_2
 0 sto sum_2
mess         ; s= #
rcl current_try 1 +
sto current_try
7 x=y goto next_try
1 sto rerun_flym
exit
lbl next_try
0 sto rerun_flym
rcl current_try
mess                 ;current_try1= #
mess                 ; next_try1
rcl test_voltage1
mess                 ; voltage1=#
exit
```

Acknowledgments

The successful accomplishment of this thesis would not be possible without support and help of many people.

Most of all I would like to express my gratitude to my supervisor Prof. E.Grün who gives me a confidence in my work.

I would like to thank Dr. R. Srama for his constant support, constructive discussions and improvements for my work.

Many thanks to Dr. Sascha Kempf and Dr. Harald Krüger for their responses and advises to my work.

Many thanks to Dmitry Khangulyan, Olivia Tsang and some others for their valuable corrections and notes.

I would like to express my gratitude to Eva Mellado for the interesting cooperation with respect to the laboratory model of the PIA/PUMA mass analyzer.

Many thanks to my neighbor, doktorand N. Altobelli also to doktorand A.Srowig, doktorand Anna Mocker-Ahlreep and all the other students who make a wonderful living and working in the Cosmic Dust Research Group at Max-Planck-Institute für Kernphysik.

Bibliography

[1] B. T. Draine and H. M. Lee. Optical properties of interstellar graphite and silicate grains. *Astrophys. J.*, 285:89–108, 1984.

[2] W. Stein. Infrared Emission by Circumstellar Dust. *ApJ*, 145:101–+, July 1966.

[3] A. Li and J. M. Greenberg. A unified model of interstellar dust. *AAP*, 323:566–584, July 1997.

[4] C. R. Chapman. Low-speed impact phenomena and orbital resonances in the moon- and planet-building process. Technical report, 1977.

[5] R. D. Gehrz. Astrophysical dust grains in stars, the interstellar medium, and the solar system. Technical report, 1991.

[6] J. I. Lunine. Physics and Chemistry of the Solar Nebula. *Origins of Life and Evolution of the Biosphere*, 27:205–224, 1997.

[7] B. Wang. Time evolution of interstellar dust and far-infrared luminosity of disk galaxies. *ApJ*, 374:456–464, June 1991.

[8] R. D. Gehrz, J. W. Truran, R. E. Williams, and S. Starrfield. Nucleosynthesis in Classical Novae and Its Contribution to the Interstellar Medium. *PASP*, 110:3–26, January 1998.

[9] Y. Sofue and K. Wakamatsu. CO in elliptical galaxies and the universal CO-to-dust ratio. *PASJ*, 45:529–538, August 1993.

[10] E. Grün, H.A. Zook, M. Baguhl, A. Balogh, S.J. Bame, H. Fechtig, R. Forsyth, M.S. Hanner, M. Horanyi, J. Kissel, B.A. Lindblad, D. Linkert, G. Linkert, I. Mann, J.A.M. McDonnel, G.E. Morfill, J.L. Phillips, C. Polanskey, G. Schwehm, N. Siddique, P. Staubach, J. Svestka, and A. Taylor. Discovery of Jovian dust streams and interstellar grains by the Ulysses spacecraft. *Nature*, 362:428–430, 1993.

[11] E. Grün, B. Gustafson, I. Mann, M. Baguhl, G.E. Morfill, P. Staubach, A. Taylor, and H. A. Zook. Interstellar dust in the heliosphere. *Astron. Astrophys.*, 286:915–924, 1994.

[12] E. Grün, H. Fechtig, R. H. Giese, J. Kissel, D. Linkert, D. Maas, J.A.M. McDonnel, G.E. Morfill, G. Schwehm, and H.A. Zook. The Ulysses dust experiment. *A&A Supl. Ser.*, 92:411–423, 1992.

[13] M. Witte, H. Banaszkiewicz, and H. Rosenbauer. Recent results on the parameters of interstellar helium from the ulysses/gas experiment. *Space Sci. Rev.*, 78:289–296, 1996.

[14] M. Baguhl, E. Grün, D. P. Hamilton, G. Linkert, R. Riemann, and P. Staubach. The flux of interstellar dust observed by Ulysses and Galileo. *Space Sci. Rev.*, 72:471–476, 1995.

[15] E. Grün, P. Staubach, M. Baguhl, D.P. Hamilton, H.A. Zook, S. Dermott, B.A. Gustafson, H. Fechtig, J. Kissel, D. Linkert, G. Linkert, R. Srama, M.S. Hanner, C. Polanskey, M. Horanyi, B.A. Lindblad, I. Mann, J.A.M. McDonnell, G.E. Morfill, and G. Schwehm. South-North and Radial Traverses through the Interplanetary Dust Cloud. *Icarus*, 129:270–288, 1997.

[16] N. Divine. Five populations of interplanetary meteoroids. *J. Geophys. Res.*, 98, 1993.

[17] P. Staubach and E. Grün. Development of an upgraded meteoroid model. *Adv. Space Res.*, 16:103–106, 1995.

[18] V. Dikarev, M. Landgraf, E. Grün, W.J. Baggaley, and D.P.Galligan. Interplanetary dust model:from micron sized dust to meteors. *Proceedings of the Meteroids 2001 Conference*, pages 609–615, 2001.

[19] E. Grün, M. Baguhl, D.P. Hamilton, R. Riemann, H.A. Zook, S. Dermott, H. Fechtig, B.A. Gustafson, M.S. Hanner, M. Horanyi, K.K. Khurana, J. Kissel, M. Kivelson, B.-A. Lindblad, D. Linkert, G. Linkert, I. Mann, J.A.M. McDonnel, G.E. Morfill, C. Polanskey, G. Schwehm, and R. Srama. Constraints from galileo observations on the origin of jovian dust streams. *Nature*, 381:395–398, 1996.

[20] H. Krüger, A.V. Krivov, D.P. Hamilton, and E. Grün. Detection of an impact-generated dust cloud around ganymede. *Nature*, 399:558–560, 1999.

[21] R. Srama, J.G. Bradley, E. Grün, T.J. Ahrens, S. Auer, A.M. Cruise, H. Fechtig, A. Graps, O. Havnes, A. Heck, S. Helfert, E. Igenbergs, E.K. Jeßberger, T.V. Johnson, S. Kempf, H. Krüger, P. Lamy, M. Landgraf, D. Linkert, F. Lura, J.A.M. McDonnel, D. Möhlmann, G.E. Morfill, G. Schwehm, M. Stübig, J. Svestka, A.J. Tuzzolino, R. Wäsch, and H.A. Zook. The Cassini cosmic dust detector. *SSR*, 2002. in press.

[22] B.-K. Dalmann, E. Grün, J. Kissel, and H. Dietzel. The ion-composition of the plasma produced by impacts of fast dust particles. *Planetary and Space Science*, 25:135–147, February 1977.

[23] E. Gruen, N. Pailer, H. Fechtig, and J. Kissel. Orbital and physical characteristics of micrometeoroids in the inner solar system as observed by HELIOS 1. *Panetary and Space Science*, 28:333–349, March 1980.

[24] H. Krueger, E. Grün, and D. P. Hamilton. Galileo in-situ dust measurements in Jupiter's Gossamer Rings. *AAS/Division for Planetary Sciences Meeting*, 35:–+, May 2003.

[25] H. Krueger and E. Gruen. Dust in the Jovian System: Streams, Clouds and Rings. *EGS - AGU - EUG Joint Assembly, Abstracts from the meeting held in Nice, France, 6 - 11 April 2003, abstract #7489*, pages 7489–+, April 2003.

[26] S. Kempf, R. Srama, N. Altobelli, S. Auer, V. Tschernjawski, J. Bradley, M. E. Burton, S. Helfert, T. V. Johnson, H. Krüger, G. Moragas-Klostermeyer, and E. Grün. Cassini between Earth and asteroid belt: first in-situ charge measurements of interplanetary grains. *Icarus*, 171:317–335, October 2004.

[27] Kissel J. The giotto particulate impact analyzer. *ESA SP-1077*, pages 67–83, 1986.

[28] Zeldovichv and Raizer. *Shock waves*. Addison-Wesley Publishing Company, INC, 1979.

[29] P.R. Ratcliff and F. Allahdadi. Characteristics of the plasma from a 94 km $s^{-}1$ micro-particle impact. *Adv. Space . Res.*, 17:87, 1996.

[30] G. Drolshagen, H. Svedhem, E. Grün, O. Grafodatsky, and U. Prokopiev. Microparticles in the geostationary orbit (GORID experiment). *Advances in Space Research*, 23:123–133, 1999.

[31] M. Stübig, G. Schåfer, R. Srama, and Grün. Laboratory simulation improvements for hypervelocity micrometeorite impacrts with a new dust particle source. *Planetary and Space Science*, 49:853, 2001.

[32] Goeller J.R. and Gruen E. Calibration of the galileo/ulysses dust detectors with different projectile materials and at varying impact angles. *Planetary and Space Science*, 37:1197–1206, 1989.

[33] R. Wieler, Th. Graf, A. Pedroni, P. Signer, P. Pellas, C. Fieni, M. Suter, S. Vogt, R. N. Clayton, and J. C. Laul. Exposure history of the regolithic chondrite fayetteville. ii - solar-gas-free light inclusions. *Geochimica et Cosmochimica Acta*, 53:1449–1459, 1989.

[34] T. J. Ahrens, S. C. Gupta, G. Jyoti, and J. L. Beauchamp. Mass spectrometer calibration of Cosmic Dust Analyzer. *Journal of Geophysical Research (Planets)*, 108:1–1, February 2003.

[35] D. Bauerle. *Laser Processing and Chemistry*. Springer-Verlag, Berlin, 1 edition, 1986.

[36] M. Dietzel, H.G. Eichhorn, H. Fechtig, E. Grün, Hoffmann H.J., and J. Kissel. The heos a-2 and helios micrometeoriod experiments. *J. Phys. E: Sci. Instrum.*, 6:209–217, 1973.

[37] B.A. Mamyrin, V.L. Karataev, D.V. Shmikk, and Zagulin V.A. The mass reflectron, a new non-magnetic time-of-flight spectrometer with high resolution. *Zh. Eksp. Teor. Fiz. and Sov.Phys-JETP*, 64 and 37:82–89 and 45–48, 1973.

[38] D.E. Brownlee, D. Burnett, B. Clark, M.S. Hanner, F. Horz, J. Kissel, R. Newburn, S. Sandford, Z. Sekanina, P. Tsou, and M. Zolensky. Stardust: Comet and interstellar dust sample return mission, in: Phys. *Chemistry and Dynamics of Interplanetary Dust, ASP Conf. Series 104, eds: B.A.S. Gustafson and M.S. Hanner, 223-226.*, 2000.

[39] Jon Ivar Øren. First order dust impact ionisation mass spectrometer - intitial energy and angular distributions of ions generated at hyper velocity impacts. Young graduate trainee report, ESTEC, Noordwijk, Netherlands, 2000.

[40] D.E. Austin, Ahrens T.J., and J.L. Beauchamp. Dustbuster:a compact impact-ionization time-of-flight mass spectrometer for in situ analysis of cosmic dust. *Review of scientigic instruments*, 73-1:185–189, 2002.

[41] J.A.M. McDonnell, J. Kissel, E. Gruen, R.J.L. Grard, Y. Langevin, R.E. Olearczyk, C.H. Perry, and J.C Zarnecki. Giotto's dust impact detection system (didsy) and particulate impact a nalyzer (pia): Interim assessment of the dust distribution and properties withi n the coma. *In ESA Proceedings of the 20th ESLAB Symposium on the Exploration of Halley's Comet. Volume 2: Dust and Nucleus p 25-38 (SEEN87-25908 19-90)*, 1986.

[42] David A. Dahl. *SIMION 3D version user's manual*. Idaho National Engineering and Enviroment Laboratory, Idaho Falls, ID 83415, 2000.

[43] Martin V. Zombeck. The high resolution camera (hrc) on the chandra x-ray observatory (cxo). Hrc home page, Smithsonian Astrophysical Observatory (Cambridge, MA), http://hea-www.harvard.edu/HRC/HomePage.html, 2003.

[44] Hamamatsu Photonics. *MCP assembly selection guide*. Hamamatsu Photonics, 314-5, Shimokanzo, Toyooka-village, Iwata-gun, Shizuoka-ken, 438-0193, Japan, 1999.

[45] M. Szilagyi. *Electron and ion optics*. Plenum Press, New York, 1988.

[46] Makarov A.A. Ideal and quasi-ideal time focusing of charged particles. *J.Phys. D:Appl. Phys.*, 24:533–540, 1991.

[47] J. Vallerga, J. Hull, and M. Lampton. Construction and evaluation of an imaging focussed-mesh electron multiplier for space instrumentation. *IEEE Transactions on Nuclear Science*, 35:539–542, February 1988.

[48] J.H Moore, C.C. Davis, and Coplan M.A. *Building Scientific Apparatus*. Addison-Wesley Publishing Company, INC, 1989.